

# Einfluss der Oberflächenrauigkeit auf die Ladung eines über die Oberfläche gleitenden Wassertropfen

## **Masterarbeit**

zur Erlangung des Grades „Master of Science“

vorgelegt von:

**Benjamin Leibauer**

Arbeitskreis Prof. Dr. Hans-Jürgen Butt

Max-Planck-Institut für Polymerforschung Mainz

Fachbereich 09: Chemie, Pharmazie und Geowissenschaften

Johannes Gutenberg-Universität Mainz

Betreuer/Erstgutachter: Prof. Dr. Hans-Jürgen Butt (Max-Planck-Institut für Polymerforschung)

Zweitgutachter: Prof. Dr. Wolfgang Tremel (Johannes Gutenberg-Universität Mainz)

Benjamin Leibauer

Matrikelnummer: 2714785

Neutorstr. 16-18

55116 Mainz

Die vorliegende Arbeit wurde in dem Zeitraum von Dezember 2021 bis Mai 2022 unter der Anleitung von Herrn Prof. Dr. Hans-Jürgen Butt und Herrn Prof. Dr. Werner Steffen an dem Max-Planck-Institut für Polymerforschung in Mainz erstellt. Nach Absprache und Genehmigung des Prüfungsamtes der Johannes Gutenberg-Universität Mainz Fachbereich 09 wurde die Arbeit auf Englisch erstellt. Eine Zusammenfassung der Arbeit in Deutsch ist ebenfalls der Masterarbeit beigelegt.

# Danksagung

Ich möchte meinen Dank zunächst in besonderem Maße **Herrn Prof. Dr. Butt** aussprechen, der mir die Möglichkeit bot, in dieses aktuelle Forschungsgebiet einzutauchen.

Ein großes Dankeschön geht an **Prof. Dr. Steffen** für die Betreuung und die Unterstützung in den letzten 12 Monaten hier am Max-Planck-Institut.

**Prof. Dr. Tremel** danke ich für die ehemalige Zusammenarbeit während der Bachelorarbeit, des Forschungsmoduls und für Ihr Zweitgutachten.

**Dr. Berger, H. Burg, F. Weber** und **P. Rohrbeck** danke ich für die Einweisung, Unterstützung und die Beantwortung meiner Fragen Rund um das Thema *AFM*.

**Dr. Kaloian** danke ich für die Diskussion über den Einfluss und die Möglichkeit zur Messung der Dielektrizitätskonstante der verschiedenen Glassubstrate auf die Ladungsmessung.

Dem **Arbeitskreis Bonn** danke ich für die Bereitstellung des *Profilometers*. **L. Prädel** danke ich für die technischen Tipps bei den Messungen.

**G. Schäfer** danke ich für die SEM-Messungen.

**P. Bista** danke ich, sowohl für die Einweisung am setup „slide electrification“ als auch für die produktiven Diskussionen Rund um das Thema „drop charge“.

**X. Li** und **S. Shumaly** danke ich für die Geschwindigkeitsmessungen und die hilfreichen Diskussionen der Ergebnisse.

**X. Zhou, F. Darvish, S. Li** und **A. Lüleci** danke ich für die produktiven Diskussionen in unseren Gruppen Seminaren.

**A. Sharifi** danke ich für die Geduld und die Zeit zur Beantwortung meiner ganzen Fragen über das Goniometer.

**M. Batzer** und **D. Cortez** danke ich für die moralische Unterstützung und das Korrekturlesen.

Für die schöne Zeit während der Masterarbeit danke ich auch **allen anderen Kollegen** der Arbeitsgruppe Butt.

Zuletzt möchte ich **meiner Familie** für die Unterstützung während des Studiums danken.

**Masterarbeit im Studiengang Chemie oder Biomedizinische Chemie  
an der Johannes Gutenberg - Universität Mainz**

---

Ich, Benjamin Leibauer, Matrikelnummer 2714785

versichere, dass ich meine Masterarbeit selbstständig verfasst und keine anderen als die angegebenen schriftlichen und elektronischen Quellen sowie andere Hilfsmittel benutzt habe. Alle Ausführungen, die anderen Schriften wörtlich oder sinngemäß entnommen wurden, habe ich kenntlich gemacht.

Mainz, 31.05.2022

(Ort, Datum)



(Unterschrift)

# Zusammenfassung

Im Rahmen dieser Arbeit wurde die Fragestellung des Einflusses der Oberflächenrauigkeit auf die Ladung eines über eine Oberfläche gleitenden Wassertropfen erörtert. Als Substrat dienten verschiedene Objektivträger aus Glas. Dabei unterschieden sich die Oberflächen der Objektivträger in ihrer chemischen Zusammensetzung.

Die Oberflächenrauigkeit wurde durch Ätzen mit Kaliumhydroxid, durch Sandstrahlen, durch Schleifen mit Silicium-Carbid Sandpapier und durch Beschichtung der Objektivträger mit Silica-Partikel verändert. Die Oberflächenrauigkeiten wurden mit dem *AFM* und einem *Profilometer* gemessen. Für die Charakterisierung wurde die root mean square (*RMS*) Rauigkeit der Oberflächen berechnet. Für die Ladungsmessung der Wassertropfen wurde die Oberfläche der Objektivträger mit einem Fluorsilan fluoriert, um eine hydrophobe Oberfläche zu erhalten.

Es konnte gezeigt werden, dass sowohl die Oberflächenrauigkeit als auch die Oberflächenchemie des Substrates die Ladung des Wassertropfens beeinflussen. Um den Einfluss der Oberflächenchemie und der Oberflächenrauigkeit separat voneinander zu erforschen, wurden in einer Messreihe die Oberflächenrauigkeit unter Erhalt der Oberflächenchemie verändert. Es konnte gezeigt werden, dass mit zunehmender Oberflächenrauigkeit die Ladung der Wassertropfen abnimmt. Um die Frage des Einflusses der Oberflächenrauigkeit genauer zu untersuchen, wurde die Geschwindigkeit der Wassertropfen auf den verschiedenen rauen Oberflächen gemessen. Es stellte sich heraus, dass die Wassertropfen auf raueren Oberflächen langsamer gleiten. Da auch die Ladung der Wassertropfen mit zunehmender Rauigkeit abnahm, konnte ein Zusammenhang zwischen Oberflächenrauigkeit, Geschwindigkeit und dem Ladungsverhalten der Wassertropfen gezeigt werden. Der Einfluss der Oberflächenchemie konnte durch das Gegenüberstellen verschiedener Substrate mit unterschiedlicher chemischer Zusammensetzung gezeigt werden. Die Oberflächenrauigkeit der Substrate lag in der selben Größenordnung, so dass ein Einfluss der Oberflächenrauigkeit auf die Ladungsmessung der Wassertropfen vernachlässigt werden konnte. Hier zeigten die Wassertropfen auf der Quarz-Glas Oberfläche die geringste Ladung. Mit zunehmender Anzahl an ionischen Verbindungen in den Glassubstraten konnte eine Zunahme der Ladung der Wassertropfen festgestellt und so der Einfluss der Oberflächenchemie auf die Ladung der Wassertropfen gezeigt werden.

# Influence of roughness on the charging of water drops moving over surfaces

In this work the question of the influence of surface roughness on the charge of a water drop sliding over a surface was discussed. Different slides made of glass were used as substrates. The surfaces of the slides differed in their chemical composition.

The surface roughness was changed by etching with potassium hydroxide, by sandblasting, by grinding with silicon carbide sandpaper and by coating the slides with silica particles. The surface roughness was measured by *AFM* and a *profilometer*. For characterization, the *RMS* roughness of the surfaces was calculated from these experiments. For the charge measurement of the water droplets, the surface of the slides was fluorinated with a fluorosilane to obtain a hydrophobic surface.

It was shown that both the surface roughness and the surface chemistry of the substrate affect the charge of the water droplet. To explore the influence of surface chemistry and surface roughness separately, a series of measurements were made to change the surface roughness while maintaining the surface chemistry. It was shown that as the surface roughness increases, the charge of the water droplets decreases. To investigate the question of the influence of the surface roughness in more detail, the velocity of the water droplets on the different rough surfaces was measured. It was found that the water drops glide more slowly on rougher surfaces. Since the charge of the water drops also decreased with increasing roughness, a relationship between surface roughness, velocity and the charge behavior of the water drops could be shown. The influence of surface chemistry could be shown by contrasting different substrates with different chemical compositions. The surface roughness of the substrates was of the same order of magnitude, so that an influence of the surface roughness on the charge measurement of the water droplets could be neglected. Here, the water droplets on the quartz-glass surface showed the lowest charge. As the number of ionic compounds in the glass substrates increased, an increase in the charge of the water droplets was observed, demonstrating the influence of the surface chemistry on the charge of the water droplets.

## Table of contents

Chapter I: Motivation .....	1
Chapter II: Fundamental Theories .....	2
2.1 Surface roughness .....	2
2.2 Interaction between solid surfaces and liquids.....	3
2.2.1 Wetting of surfaces .....	3
2.2.2 Electric double layer .....	5
2.3 Slide electrification.....	8
2.4 Silanization/Fluorination .....	10
Chapter III: Experimental part .....	12
3.1 General procedure: .....	12
3.2 Substrate material: .....	12
3.3 Fluorination .....	14
3.3.1 Sample pre-preparation .....	14
3.3.2 Fluorination .....	14
3.3.3 Silica particles .....	15
3.4 Etching .....	16
3.5 Sandblasting .....	16
3.6 Sandpaper.....	17
3.7 Measurement RMS roughness .....	17
3.8 Charge measurement .....	18
3.9 Contact angle goniometer .....	20
3.10 Scanning electron microscope .....	23
3.11 Velocity measurements.....	23
Chapter IV: Results and discussion.....	25
4.1 Changing surface roughness.....	25
4.1.1 Etching .....	25
4.1.2 Sandblasting .....	26



4.1.3 SiC-sandpaper.....	27
4.1.4 Coating with silica particle.....	28
4.1.5 Results and discussion of the calculated <i>RMS</i> roughness .....	29
4.2 Charge measurement .....	31
4.3 Influence of roughness on the charge measurement .....	36
Chapter V: Summary .....	40
5.1 Conclusion .....	40
5.2 Outlook.....	40
CHAPTER VI: Chemicals .....	41
Chapter VII: Lists.....	42
7.1 List of abbreviations .....	42
7.2 List of figures .....	43
7.3 List of tables.....	50
Chapter VIII: Literature.....	51
8.1 References.....	51
Chapter IX: Appendix.....	53

## Chapter I: Motivation

In current research, many new ways are being explored worldwide to generate energy in an environmentally friendly way. An alternative to solar and wind energy is the generation of electricity by means of hydroelectric power.<sup>[1]</sup> In addition to generating energy from flowing water through turbines, another possibility is to generate electricity through individual water droplets.<sup>[2]</sup> This enables energy generation from raindrops or wastewater.<sup>[3]</sup> Around ten years ago, some groups succeeded in harvesting electrical energy by different methods.<sup>[1]</sup> J. Moon et al. showed that it is possible to generate an AC current when the water flows between two conducting plates.<sup>[4]</sup> Further work showed that electric energy can also be generated by sliding water over hydrophobic surfaces.<sup>[5]</sup> Many triboelectric nanogenerator (**TENG**) have been presented here in recent years.<sup>[6]</sup> In some publications light-emitting diodes (**LED**) could be operated by water drops.<sup>[7]</sup> In the case of the *TENG* the current is generated by contact electrification.<sup>[8]</sup> The effect of the contact electrification is known since ancient times.<sup>[9]</sup> Thales of Miletus (around 540 BC) discovered the effect of contact electricity when he rubbed amber against wool.<sup>[10]</sup> This effect is also very well known in everybody life. Well known examples are that we sometimes get a small electric shock when we touch metallic door handles or that a balloon rubbed on hair will stick to the hair.<sup>[11]</sup> Reason is that after rubbing, the two objects are electrically charged.<sup>[12]</sup> This kind of contact electrification is caused by the triboelectric effect. The term “triboelectric” comes from the Greek and translated in the Greek language the term would mean “rubbing amber”.<sup>[11]</sup> The triboelectric effect describes that after two objects are rubbed together and then separated the two objects are loaded.<sup>[13]</sup> Although the contact electrification is widely used in photocopying, laser printing, electrostatic separations and chemical systems, the physical processes are still being discussed today and many question such as what causes surface to charge or what species are transferred to generate the charge have not yet been clearly clarified.<sup>[14]</sup> To investigate these questions in more detail, the charge of single drops sliding down a surface can be measured. For this purpose Stetten et al. established a new experimental setup which it is possible to measure the charge of single water drop.<sup>[15]</sup> In this way, the influence of the droplet properties and the surface properties on the charge separation can be investigated separately. Further studies have already shown that the drop charge depends, among other things, on the surface chemistry.<sup>[16]</sup> Other chemical and physical droplet properties such as *pH* value, influence of dissolved salts or droplet velocity can be researched independently of each other.

The motivation of this work is to extend the understanding of charge separation from water drops on hydrophobic glass surfaces. The influence of the surface roughness on the drop charge is to be investigated. In order to discuss the question, the first task is to change the surface roughness of glass slides and characterize the surface roughness. The *root mean square (RMS)* roughness is used to

determine the surface roughness. In a second step, the drop charge on the different surfaces of different roughness and partly different chemical composition is measured and discussed.

## Chapter II: Fundamental Theories

### 2.1 Surface roughness

Surface physics describes physical and chemical phenomena on the surface of a solid. There are a lot of different surface properties which influence processes such as adsorption or wetting. One of these properties is the *surface roughness*. The surface roughness correspond to the height profile of a surface.<sup>[17]</sup> Figure 1 (a)) represents the image of a surface, recorded with the *atomic force microscope (AFM)*. To analyze the surface roughness we can measure the height profile at different points on the surface (Figure 1). When we compare the two measured height profiles we see that the two extracted height profiles show different levels of surface roughness (black and red height profile in Figure 1 b)). This shows that the calculation of the surface roughness depends first of all on the measuring distance.<sup>[18]</sup> Furthermore the measured height profile must be evaluated to obtain a value for the surface roughness. From the height profile in Figure 1 (b)) the statistical character of the surface roughness becomes obvious. There are several ways to calculate the surface roughness from the recorded height profile.<sup>[19]</sup> One opportunity for the calculation is the average roughness parameter  $R_a$ . This parameter indicates the mean distance of the actual surface height from the mean contour line. Here the center line is placed in such way that the sum of the height deviations assumes the smallest value. The average roughness parameter is used less. More common is the use of the  $R_q$  parameter (*root-mean-square roughness (RMS)*) to calculate the surface roughness. This parameter is equal to the square root of the sum of the squares of the deviations from the mean contour line. Equation 1 shows the formula for the calculation of the  $R_q$  parameter.<sup>[18]</sup>

$$R_q = \sqrt{\frac{1}{MN} \sum_{m=1}^M \sum_{n=1}^N (z(x_m, y_n) - \langle z \rangle)^2}$$

*Equation 1: This equation shows the calculation of the root-mean-square parameter  $R_q$  (RMS). The parameter  $z$  represents the value of the height.  $M$  and  $N$  represent the number of points in  $x$  and  $y$  direction.*

Equation 1 is used to calculate the surface roughness. The calculation of the *RMS* values is performed by the software of the used device.

Next to the different calculation options there are different devices to measure the surface roughness. One possibility is the *AFM*. Here are different measuring modes possible. For this master thesis the

tapping mode is used (chapter 3.7 Measurement RMS roughness).<sup>[20]</sup> Other methods are the *scanning electron microscope (SEM)* or a polarization microscope to measure the surface roughness.<sup>[21]</sup> Besides to the *AFM* a *profilometer* is used to detect the surface roughness (chapter 3.7 Measurement RMS roughness). In contrast to the *AFM* the measurement takes place in only one direction and larger scan sizes are possible. Similar to the *AFM* in contact mode a force is applied between the measuring tip and the surface. During the scanning a force-distance course is recorded and a height profile is obtained.<sup>[20]</sup>

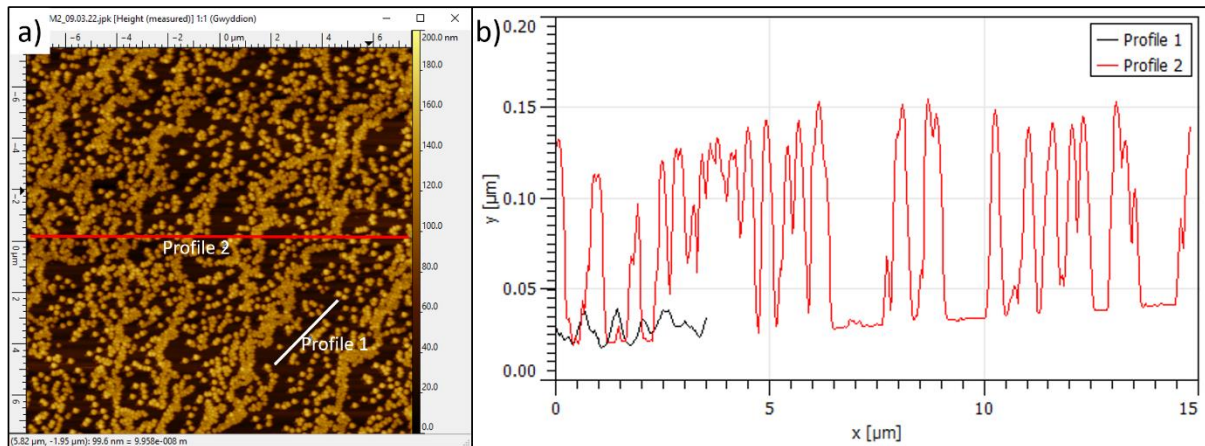


Figure 1: Illustration of the surface roughness. a) The surface was measured with the AFM at a scan size of 15  $\mu$ . Along two lines in the image (red and white line) a height profile was recorded as shown in b). The red plot corresponds to the red line in a) (RMS roughness=31.2 nm). The black plot in b) corresponds to the white line in a) (RMS roughness=4.7 nm). A comparison of these two profiles in b) shows that the surface roughness is dependent both on the point of the measurement and the scan size. The scan size has always be cited to make the results comparable. A number for the surface roughness can be calculated from the high profile. Here are different methods of the calculation of the surface roughness possible.

## 2.2 Interaction between solid surfaces and liquids

### 2.2.1 Wetting of surfaces

Interaction between a liquid and a solid surface is an interesting and topical field in the world of surface chemistry and solid state physics. There a lot of effects and possibilities to describe this topic. Therefore, only the interactions relevant to this master thesis will be discussed. A deeper insight into surface physics can be taken from the given references.<sup>[22]</sup> An important topic for this work is the wetting properties of surfaces with water.

In general the wetting properties are important for a lot of applications in science and industry.<sup>[23]</sup> Examples of industrial processes are painting and printing of all kinds of surfaces.<sup>[24]</sup> Examples for the application in daily life and research are water repellent fabrics and self-cleaning surfaces. In this context, the best known example is probably the *lotus effect*.<sup>[25]</sup>

The first who describes the wetting properties of solid surfaces physically was Thomas Young in the year 1805.<sup>[26]</sup> He introduced the *contact angle (CA)* to characterize the wetting properties of surfaces

(Figure 2, a)).<sup>[27]</sup> He related the *CA* to the thermodynamic equilibrium of the surface tension  $\gamma$  between the different media solid, liquid and vapor ( $\gamma_{SV}$ - surface tension solid-vapor;  $\gamma_{LV}$ - surface tension liquid-vapor and  $\gamma_{SL}$ -surface tension solid-liquid, see Figure 2, a)). The model is shown schematically in Figure 2 (a)).<sup>[26]</sup> This model describes an ideal surface (physical and chemical homogenous). The measurement of the *CA* is called the *static contact angle (SCA)*. In a lot of publications the *SCA* is used to characterize the wetting properties of surfaces. Disadvantage from the *SCA* is that the *SCA* assumes that the drop would be in a global energy minimum. That means, according to the Young model, that the drop would be in a steady state. But since the surface has defects, the drop size is dependent on the humidity of air and room temperature and so the drop could be in any local energy minimum. Therefore the measurement and calculation of the *SCA* can extend over a measuring range and the *SCA* is not necessarily reproducible.<sup>[24]</sup> To avoid this the *advancing contact angle (ACA)* and the *receding contact angle (RCA)* can be analyzed. In Figure 2 (b) the *ACA* and *RCA* of a moving drop are presented. The *ACA* and the *RCA* can be measured by first increasing and then decreasing the volume of the drop (cf. chapter 3.9 Contact angle goniometer). During the drop size get increased the *CA* of the drop front increased and the front of the drop starts to move till the *CA* reaches a maximum. This maximum angle is the *ACA*. When the volume of the drop gets decreased the *RCA* can be calculated.<sup>[28]</sup> The *RCA* is defined as the *CA* when the drop front starts to move during the volume of the drop gets reduced.<sup>[24]</sup> In general, we can say that the advancing of a liquid is related to the wetting of additional surface area and the receding motion is associated with the dewetting of the surface. The difference between *ACA* and *RCA* is called *contact angle hysteresis (CAH)*. The *CAH* can be used for the description of the mobility of a drop on a surface.<sup>[29]</sup> With increasing of the *CAH* the drop mobility decrease. Thus the *ACA*, *RCA* and *CAH* are used to describe the motion of drops.<sup>[28]</sup>

Furthermore, properties such as the surface roughness are neglected in model of Young.<sup>[30]</sup> The influence of the surface roughness to the *CA* was added from Wenzel. For this purpose, he introduced a roughness factor that describes the ratio between actual *CA* (apparent *CA*) and geometrical *CA* (Young *CA*).<sup>[31]</sup> Here the actual *CA* is the measured. Figure 2 (c, d) show that there are two different states of wetting are possible. If there is no air between drop and surface we call this state *Wenzel state* (Figure 2 c)).<sup>[30]</sup> Is there air between drop and surface the so called Cassie-Baxter equation is fulfilled and the drop is in the so called *Cassie-Baxter State* (Figure 2 d)).<sup>[32]</sup>

With the help of the *CA*, surfaces can be divided into different classes. We call surfaces *hydrophilic* when the *CA* is smaller than 90°. If the *CA* is between 90° and 150° the surfaces have *hydrophobic* properties. We call surfaces with a *CA* larger than 150° *super hydrophobic*.<sup>[27]</sup>

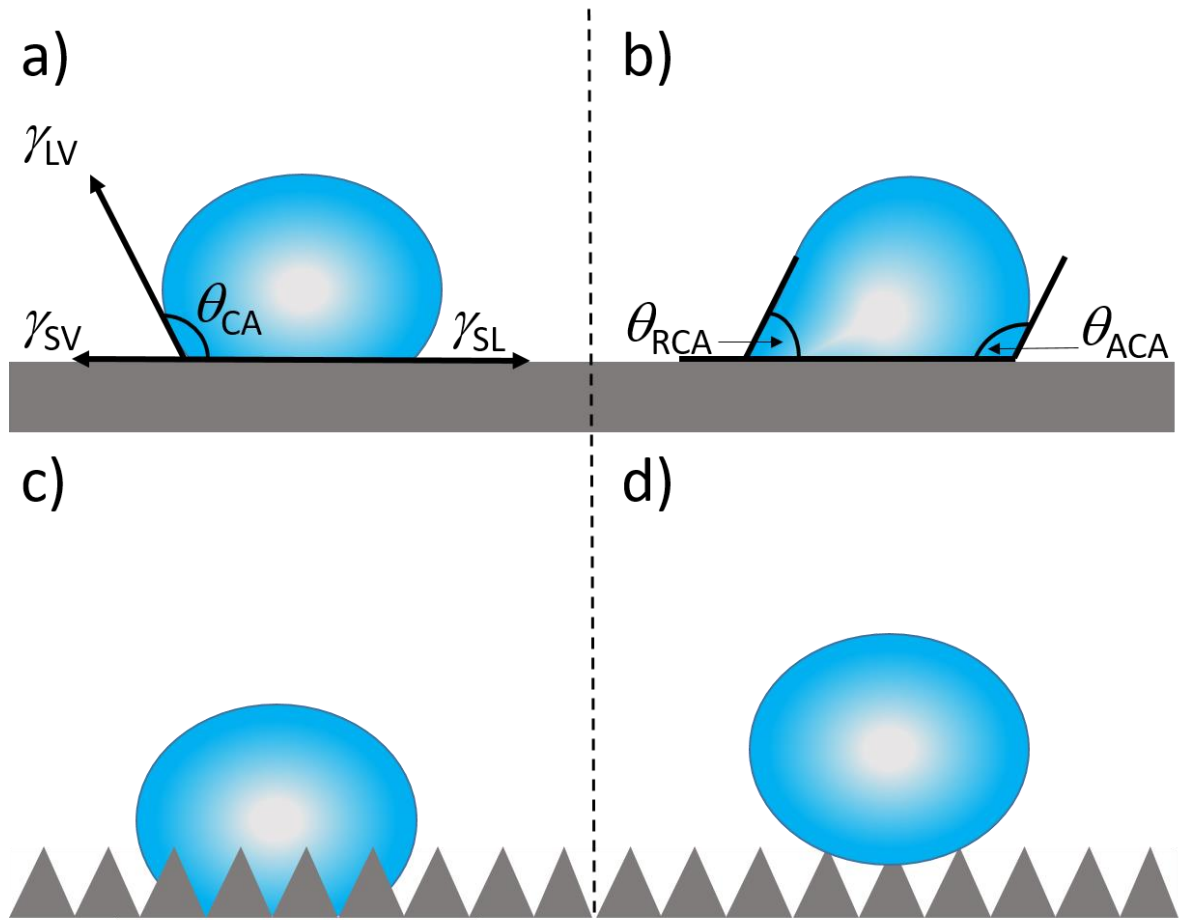


Figure 2: Schematic illustration of the definitions of the contact angle, the advancing and receding contact angle and the wetting state in dependence on the surface roughness. a) Represents the Young model, which is used to describe the wetting properties with the contact angle ( $\theta_{CA}$ ) and the surface tension  $\gamma$ . The contact angle is the angle between the surface and the front of the water drop, when the drop is in a thermodynamic equilibrium. The thermodynamic equilibrium means that the surface tension between the three media solid, air (vapor) and liquid ( $\gamma_{SV}$ - surface tension solid-vapor;  $\gamma_{LV}$ - surface tension liquid-vapor and  $\gamma_{SL}$ -surface tension solid-liquid) are in an energetic equilibrium state. The Young model describes ideal surfaces. b) Advancing (ACA) and the receding contact angle (RCA) of a moving drop. The right drop front represents the front in which the drop moves. The maximum contact angle is called ACA ( $\theta_{ACA}$ ). On the left side, we see the angle from the front which is receding. The angle at which the droplet starts to move is the RCA ( $\theta_{RCA}$ ). Under consideration of the surface roughness, there are two different states of wetting possible. c) Shows the Wenzel state. In this state no air is between drop and surface. d) Shows the Cassie-Baxter state. In this case air is between the surface and the drop.<sup>[27]</sup>

### 2.2.2 Electric double layer

Another relevant topic for the interaction between solid surfaces and liquids is the *electric double layer (EDL)*. The formation of an absorption layer of dissolved ions and some molecules at a phase interphase (solid/liquid, solid/vapor or liquid/vapor) is generally associated with the occurrence of a potential difference. The potential difference is referred to as the zeta potential.<sup>[33]</sup> Since this work focuses on the interaction between water drops and a fluorinated glass surface, we will not go into further detail at this point about the interaction at the liquid/vapor and solid/vapor phase interphase. In fact, due to the high dielectric constant of water, most of the ions are dissolved in water and most of the surfaces

are charged when in contact with water. Surface charges cause an electric field which attracts counter charge or counter ions.<sup>[22]</sup> This interaction forms the previously mentioned absorption layer at the interface between water and the solid surface.<sup>[33]</sup> This layer is called *EDL*. The *EDL* is shown schematically in Figure 3. The counter ions which bind directly to the surface and neutralize the surface charge is called the *inner Helmholtz plane (IHP)*. Solvated molecules can attach to this *IHP* and form the so called *outer Helmholtz plane (OHP)*.<sup>[34]</sup> Helmholtz treated the *EDL* as a parallel-plate capacitor. One plate corresponds to the charged interface between water and the solid surface. The second plate correspond to the center of the closest-approaching hydrated counter ions (*OHP*).<sup>[35]</sup> With the Helmholtz model some basics of charged surfaces could be explained. But the model cannot explain the capacitance of an electric double layer.<sup>[22]</sup> The reason for this is that the *EDL* is regarded as a rigid layer and the thermal movement of the solvent molecules and the ions are not taken into account.<sup>[36]</sup> The model was extended to explain this by Gouy, Chapman and Stern. In consideration of the thermal fluctuations the counter ions can diffuse away from the surface and form a diffuse layer.<sup>[22]</sup> The Stern layer describes the *IHP* as a rigid layer and the *OHP* as the diffuse layer. Depending on the thickness of the Stern layer and the diffuse layer the potential can be described as a function of the distance from the surface (Figure 3).<sup>[35]</sup> For a deeper insight see the reference.<sup>[22]</sup>

The fact that in this master thesis the drop charge of highly purified Milli-Q (18.2MΩcm) water is measured and the paradigm of electro neutrality assumed in the *EDL* theory<sup>[15]</sup> brings some questions like for example what is the origin of the drop charge. This is to be discussed in more detail at this point.

Since Milli-Q water is used, it can be assumed that the water does not contain any ions. Impurities or contamination are to be neglected. The autoprotolysis of water allows a proton to be transferred from one water molecule to another ( $2 \text{H}_2\text{O} \rightleftharpoons \text{HO}^- + \text{H}_3\text{O}^+$ ). If the *pH* value is less than or greater than seven, more oxonium ions ( $\text{H}_3\text{O}^+$ ) or hydroxide ( $\text{HO}^-$ ) ions are present and the water is charged.<sup>[37]</sup> The used Milli-Q water has a *pH* value of seven (6.998).<sup>[38]</sup> That means the water has no formal charge. However, the water is pumped through a tube. A metallic grounded needle is attached to the end of the tube to apply the drops to the surface (cf. chapter 3.8 Charge measurement). Here, too, an *EDL* is formed between the tube, the needle and the water. Due to the *EDL* in combination with the autoprotolysis of the water, charges can be present in the water drops and influence the drop charge. The *pH* value of the water drops applied to the surface is not known since our lab-pH meters are not precise enough. After producing the Milli-Q water and during the drop charge measurement, the Milli-Q water is exposed to air. During this time, gases such as oxygen, nitrogen or carbon dioxide ( $\text{CO}_2$ ) can dissolve in the water and influence the *pH* value.<sup>[39]</sup> Nitrogen and oxygen are poorly soluble in water<sup>[40]</sup> and therefore the influence of the two gases on the *pH* value of water should be neglected.  $\text{CO}_2$  is well

known to lower the *pH* of water.<sup>[41]</sup> CO<sub>2</sub> can react with water to carbonic acid and the carbonic acid can disassociate in hydrogen carbonate and a proton ( $\text{H}_2\text{O} + \text{CO}_2 \leftrightarrow \text{H}_2\text{CO}_3 \leftrightarrow \text{H}^+ + \text{HCO}_3^-$ ).<sup>[37]</sup> Charges are present in the water drops due to the hydrogen carbonate and the lower *pH* value. P. Vogel et al.<sup>[39]</sup> showed that the CO<sub>2</sub> in water influence the zeta potential of fluorinated glass surfaces. The fluorinated glass surfaces, similar to our f-slides, had a negative zeta potential.<sup>[39]</sup> The fluorinated glass surfaces are probably negatively charged due the absorption of hydroxide ions.<sup>[15]</sup> Here the question arises why a hydroxide ion is absorbed. Surface defects may be compensated by the absorption. It is known that the drop charge is also influenced by chemical reactions.<sup>[16]</sup> Fluorosilane with chlorine groups is used for the fluorination of the glass slides (chapter 3.3 Fluorination). After the reaction chlorine signals were detected via TOF-SIMS<sup>[42]</sup>; here the substrate was the photoresist SU-8 which does not contain chlorine atoms as constituents. This could mean that after the synthesis there are still free chlorine groups. The free chlorine group can react with water ( $\text{R-Cl} + \text{H}_2\text{O} \rightarrow \text{HCl} + \text{R-OH}$ ) and form hydrochloride acid. The hydrochloride acid would decrease the *pH* value and also chloride ions are present. This would be influences the drop charge.



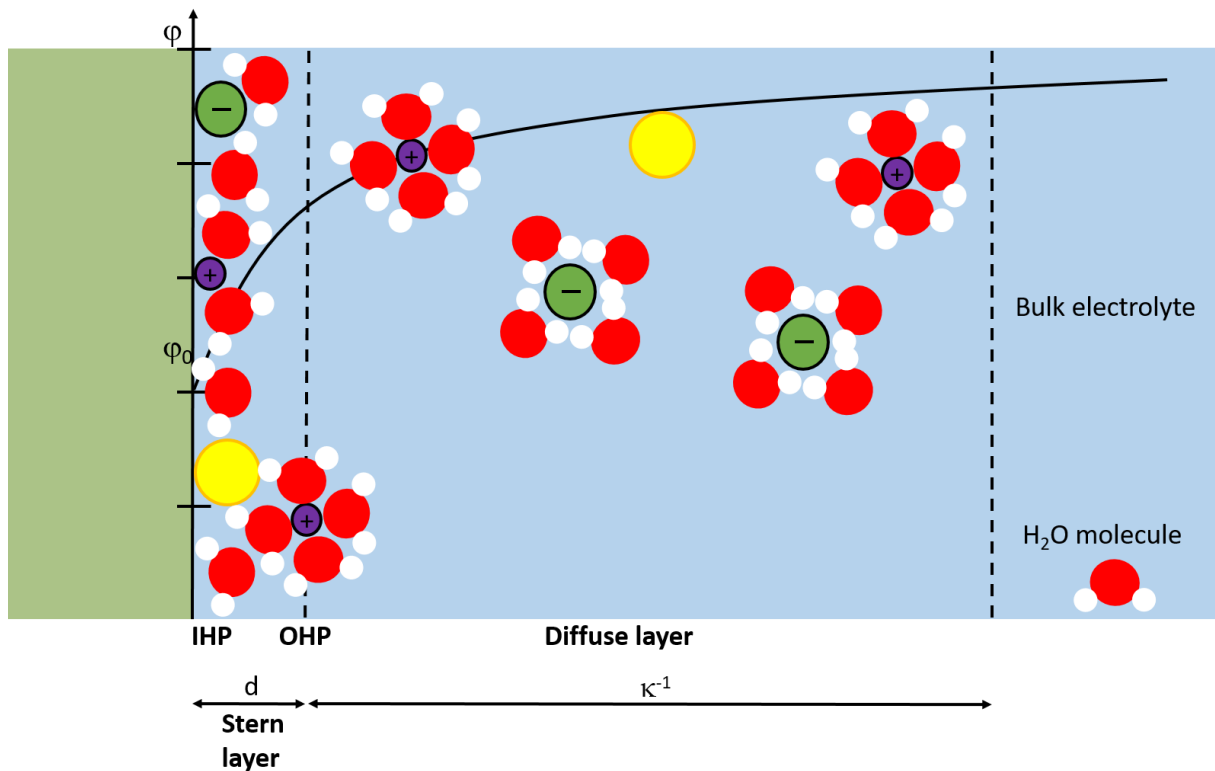


Figure 3: Schematic illustration of the electrical double layer (Gouy-Chapman-Stern model). The green bar on the left side represents the solid. Blue background represents the liquid medium (e.g. water). The yellow, green and purple spheres represent the neutral species, the anions and the cations. The ions are solvated by water molecules (red: oxygen, white: hydrogen). The inner Helmholtz plane (IHP) describes the interaction between the surface of the solid and the liquid medium. In fact, of the surface charge counter ions and counter charge bind to the surface to neutralize the charge. Also, solvent molecules like the water molecules can adhere to the surface to neutralize the surface charge. The outer Helmholtz plane (OHP) describes the interaction of solvated molecules with the IHP. Together, these both layers form the so called Stern layer. The Stern layer is bordered by the diffuse layer. Since the ions or solvated molecules diffuse from the Stern layer to the diffuse layer and vice versa a potential  $\phi$  can be described as a function of the thickness of the Stern layer ( $d$ ) and the distance from the surface. The diffuse layer is also called Debye length ( $\kappa^{-1}$ ).<sup>[35]</sup>

### 2.3 Slide electrification

Electrical energy can be obtained through the interaction between liquids and surfaces. Here kinetic energy is converted into electrical energy.<sup>[43]</sup> To understand this in more detail the charge of a water drop sliding down a hydrophobic surfaces can be measured and analyzed. Since the hydrophobic surface of microscopic glass slide is used here, we can speak of *slide electrification*.<sup>[15]</sup>

The measured charge of the water drops is called **drop charge** in the following. To obtain the drop charge the current of each moving drop get detected with an electrode (Figure 4 a)). By integration of the current signal over the discharging time the drop charge can be determined (Figure 4 b)). Here the discharging time of the water drop at the electrode is taken as the time interval for the integration (between 0 and 20 ms). The drop charge from the first drop is larger than the drop charge of the subsequent drops (Figure 4). The drop charge is decreasing with increasing drop number. After around

200 drops a constant drop charge is measured (Figure 4, b), blue circle). The drop charge from this point is called *saturation charge*. For the discussion of the results the saturated charge is used. The sign of the measured current gives us information about the interaction between drop and surface. A negative current means that the drop has a negative charge and the electrons flow from the drop to the electrode. From this can be derived that in this case a positive charge of the water drop left on the surface (e.g.  $\text{H}_2\text{O} \leftrightarrow \text{H}^+ + \text{HO}^-$ ) and the drop is negatively charged.<sup>[15]</sup> By functionalizing the surface chemistry, the sign of the drop charge can be changed and this shows us that one explanation for the measured charge is the chemical interaction between the drop and the surface.<sup>[16]</sup>

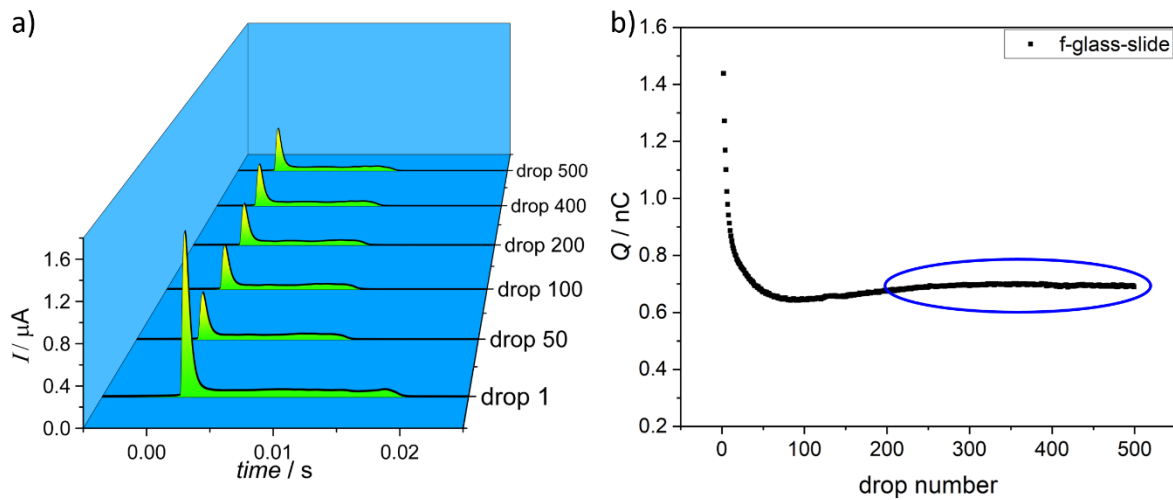


Figure 4: Calculation of the drop charge. The results of the drop charge measurement of 500 water drops sliding over a fluorinated glass slide surface should serve as an example. During the measuring the current of each drop is measured with an electrode. a) Detected current signal for drop number: 1, 50, 100, 200, 400, 500. With an increasing drop number the current of the drop first decrease till the current takes on a constant value around drop number 200. Furthermore follows from the plot the discharging time of the drop at the electrode. The whole discharging time of the drop is around 20 ms. For the calculation of the drop charge, the current signal is integrated over the time ( $Q = \int I(t) dt$ ). The time interval for the integration is given by the discharging time of the current peak (around 0.2 ms). b) The calculated drop charge is plotted against the drop number. With an increasing drop number the drop charge decrease till the drop charge reach a constant value. The drop charge at this point is called saturation charge (saturated charge) (blue circle).

Furthermore, the following model can be used to describe the slide electrification (Figure 5). Here the whole drop charge process can be divided in three steps. The first step describes the spontaneous charge formation in an aqueous sliding drop ((1) in Figure 5). The second step is the transfer of charge from the drop to the surface (see (2) in Figure 5). The third step represents the neutralization of the surface charge. That can be achieved through processes such as flow of electrons (electrically conductive substrates) through the grounded substrate or by ions in the air ((3) in Figure 5).

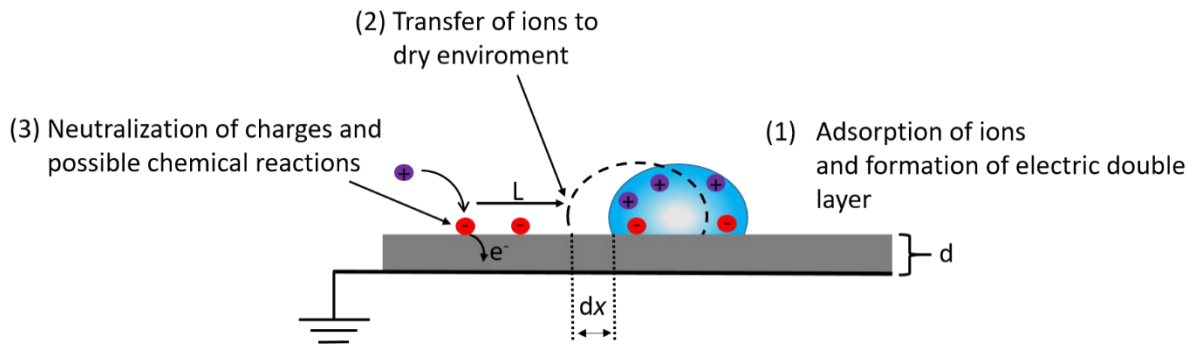
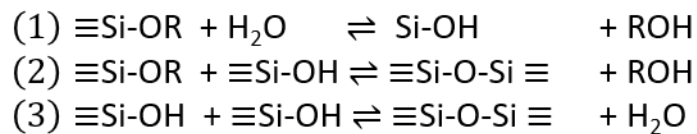


Figure 5: Schematic model for the description of the slide electrification. The model is divided into three steps to explain the whole charging process of a water drop sliding down a hydrophobic surface. (1) The interaction between the droplet and the solid surface leads to the formation of an electric double layer. (2) Charges are transferred to the surface. When the drop continues to slide the charges remain on the surfaces. (3) The surface charge can be neutralized through various possibilities. The neutralization of the charge can be done by e.g. by ions from the air, interaction with the next drop or by flow of electrons through the grounded substrate.<sup>[15]</sup>

## 2.4 Silanization/Fluorination

Silanization offers an interesting and in science and industry common method to change the surface properties of glass. This reaction is used to change the surface chemistry of silica particles, silicon dioxide or silicon wafer.<sup>[44]</sup> This modification enables to manipulate the wetting properties of these surfaces. One common method is the silanization with fluorine containing oligomers to change the wettability of the surface. Here e.g. hydroxyl groups (**OH**) on the surface of a glass reacting area with a reagent used such as the reaction between quartz glass and trichloro-(1H, 1H, 2H, 2H-perfluorooctyl)-silane (**PFOTS**) in Figure 6.<sup>[45]</sup> Interesting group of reagents are silanes. These are a class of organosilicon molecules which offer a wide range of compounds because the side groups can be easily chemically modified. On this way, the reaction can be used to specifically influence the surface of glass.<sup>[46]</sup> Silanization can generally be described by three reactions. These are shown in Equation 2.<sup>[47]</sup>



Equation 2: Reaction equation of silanization. The following reaction types describe the silanization: (1) Hydrolysis: An alcohol group of a silane (OR) reacts with water (H<sub>2</sub>O). On this way the hydroxide group (OH) is bonded to the silane during an alcohol (ROH) leaves the reaction. (2) Alcohol condensation: A silane with an alcohol group reacts with a silane with a hydroxide group. Here two silanes are bonded together under alcohol separation. (3) water condensation: The hydroxide groups of two silanes interact among themselves and two silanes get bonded under water separation.<sup>[47]</sup>

The first reaction equation describes the hydrolysis of the alkoxide groups (**OR**). These groups are replaced by hydroxyl groups (OH). Condensation allows the silanes to polymerize and form chains and network structures. Here a distinction can be made between alcohol and water condensation. Alcohol

condensation describes the interaction between an alkoxide and the hydroxyl group. Here an alcohol (**ROH**) is split off while two silanes get connected. Water condensation describes the interaction between two hydroxyl groups. During the reaction a water molecule is set free when two silanes get bonded.<sup>[47]</sup>

In this work the silanization is used to change the hydrophilic character of glass into a hydrophobic one. Since in my work a silane with fluorine groups is used, the reaction is referred to in the following as **fluorination**. Figure 6 shows the fluorination of quartz glass with PFOTS schematically. The reaction initiated via chemical vapor deposition (**CVD**) and is carried out in two steps as described above (hydrolysis and condensation).

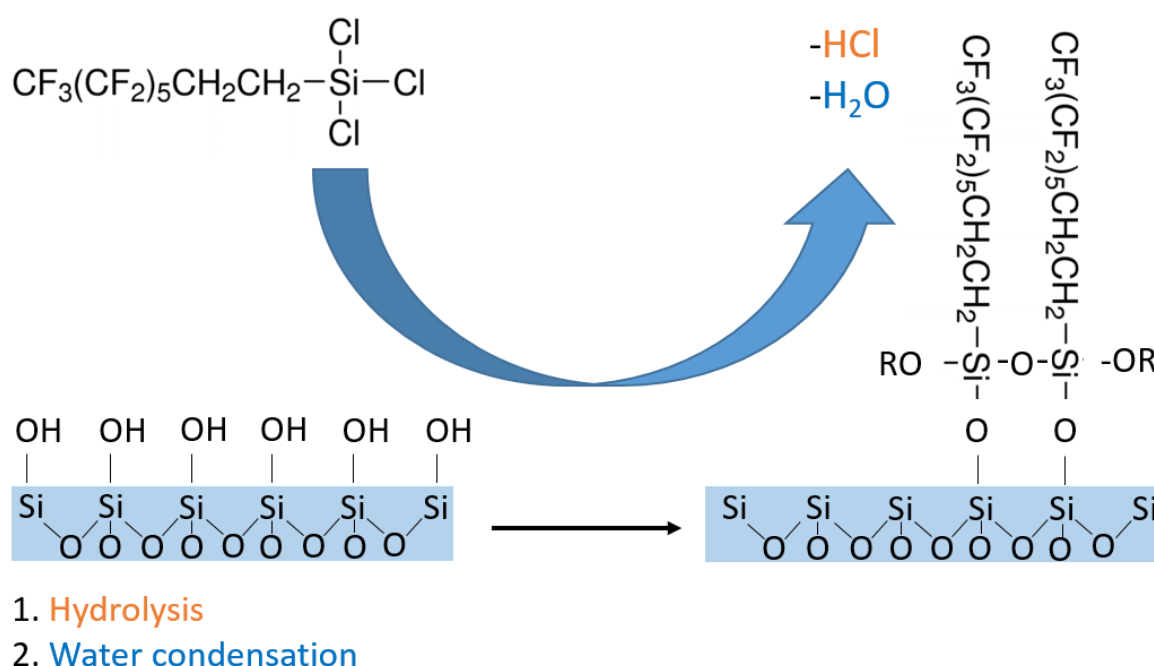


Figure 6: Schematic diagram of the fluorination of quartz glass. The fluorination reagent is 1H,1H,2H,2H-perfluorooctyltrichlorosilane (**PFOTS**). First, hydrolysis of the PFOTS lead to the elimination of hydrogen chloride (HCl). The hydroxide group of the PFOTS can now interact with hydroxide groups of the quartz-glass. Water ( $\text{H}_2\text{O}$ ) is released as bye-product in this process (condensation). Also condensation is then used to bond the silane chains between each other to the glass surface.

## Chapter III: Experimental part

### [3.1 General procedure:](#)

All experiments were done three times at three different days on different samples. The average of the experiments was used for the evaluation. Errors were calculated by means of standard deviation. The calculations were performed with *Microsoft Excel 2016*, *Origin 2021*, *Gwyddion 2.59*, *ImageJ 1.53k*, *Matlab* and *Python*.

### [3.2 Substrate material:](#)

Three different substrate materials were used. The bulk of this master thesis was done on so called microscope slides (Thermo Fisher scientific Gerhard Menzel B.V. & Co. KG, Braunschweig, Germany) used as substrate. The dimension of the microscope slides are 26 x 76 x 1 mm. In the following, the “Menzel” microscope slides are referred as **slide** and fluorinated slides as **f-slide**. The chemical composition of the slides is summarized in Table 1.

*Table 1: The chemical components of the microscopic slides (Thermo Fisher scientific Gerhard Menzel B.V. & Co. KG).*

chemical component	fraction / %
SiO <sub>2</sub>	72.20
MgO	4.30
Na <sub>2</sub> O	14.30
Al <sub>2</sub> O <sub>3</sub>	1.20
K <sub>2</sub> O	1.20
Fe <sub>2</sub> O <sub>3</sub>	0.03
CaO	6.40
SO <sub>3</sub>	0.30

Figure 7 shows the *AFM* images of a pristine and a fluorinated slide. A comparison of them shows that there is no visible influence of fluorination to the surface in terms of structures. The *RMS* roughness of the slide before and after fluorination was of the same order ( $(0.5 \pm 0.1) \text{ nm}$ ). Therefore we can safely assume a monomolecular layer of the fluorination compound. Both images show the common pattern of the slide surface (circle in Figure 7). These pattern were observed in all measured slides. It is obviously that these patterns are different (blue vs. red circle in Figure 7). These images showing the difference of glass on a microscopically level. The reason for the differences lies in the manufacture. In each slide the molten glass had a microscopically different composition and different conditions

during cooling so every glass is microscopically different.<sup>[48]</sup> This shown that the properties and chemical composition on the surface of glass could differ from slide to slide.

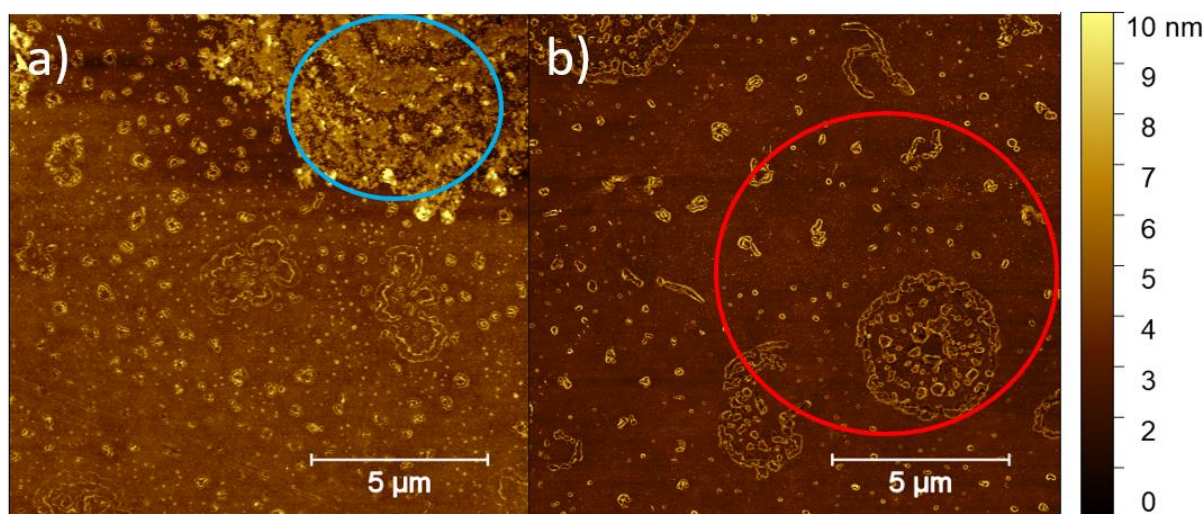


Figure 7: AFM images of a) pristine and b) fluorinated slide. The pattern (e.g. red and blue circle) on these images were observed on all measured slides. A comparison of the pattern in a) and b) shows that the surface structures from slide to slide are different. Furthermore the comparison between a) and b) shows that the fluorination has no visible influence to the surface structure and such an influence to the surface roughness can be neglected (RMS roughness from a) and b) are in the same order of magnitude ( $0.5 \pm 0.1$  nm)). The images were recorded at a scan size of  $15 \mu$ .

Additionally N-LASF45 (Schott AG, Mainz, Germany) glass slides and substrates made from quartz glass (Thermo Fisher Scientific, USA) were used. The dimension of the N-LASF45 glass slide were  $25.1 \times 76 \times 1.5$  mm, the exact chemical composition is a trade secret of the company Schott. The dimension of the quartz glass slides were  $25.4 \times 76.2 \times 1$  mm. The AFM images of the quartz glass slide and N-LASF45 glass slide are summarized in Figure 8. In contrast to the “Menzel” glass slides a pattern due to the different components of the glasses are not visible (cf. Figure 7 and Figure 8).



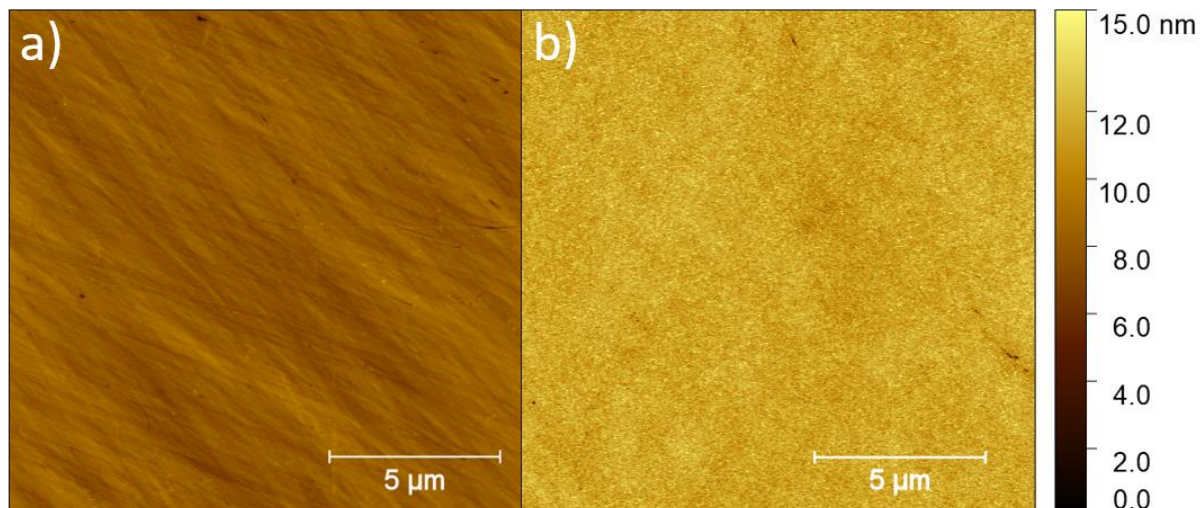


Figure 8: AFM images of a) quartz glass slide and b) N-LASF45 glass slide. The images were recorded at a scan size of  $15\ \mu$ . In contrast to the “Menzel” glass slides no different patterns are visible (see Figure 7). The calculated RMS roughness is for a)  $(0.5\pm0.1)\text{ nm}$  and b)  $(0.7\pm0.1)\text{ nm}$ .

### 3.3 Fluorination

#### 3.3.1 Sample pre-preparation

Before silanization the samples were cleaned with ethanol (absolute, Honeywell) in an ultrasonic bath for 15 min to remove any lubricant and dust from the production process. In a further cleaning and activating step (protonation of the OH-groups), the slides were cleaned with hydrochloric acid (37 %, Sigma Aldrich) in methanol (absolute, VWR) (ratio 1:1) for 30 minutes.<sup>[45]</sup> Subsequently, the surface was treated with oxygen plasma (Diener electronic Femto, Plasma-Surface-Technology, Ebhausen, Germany,  $6\text{ cm}^3\text{ min}^{-1}$  oxygen flow rate, 120 W) for 2 min at 120 W to remove organic contaminations and further enhance the number of OH-groups.<sup>[49]</sup>

#### 3.3.2 Fluorination

The samples were fluorinated with 1H, 1H, 2H, 2H-Perfluorooctyltrichlorosilane (PFOTS, 97%, Alfa Aesar). Fluorination was carried out according to an amended test specification of W. Munief et al. via CVD to coat the slides.<sup>[46]</sup> The slides were placed directly into a glass desiccator. 1 mL of PFOTS was prepared in a glass petri dish ( $d = 6\text{ cm}$ ;  $h = 1\text{ cm}$ ). The reaction was done at a pressure of less than 200 mbar for one hour at room temperature. A magnetic stirrer was used to enhance air circulation (150 rpm). After reaction, the samples were rinsed with ethanol and DI water ( $18\text{ M}\Omega\text{cm}$ ). The slides were dried with nitrogen gas and subsequent two hours in desiccator at less than 100 mbar.

The fluorination was observed with AFM. The results are summarized in Figure 9. After the fluorination with PFOTS the surface is covered completely with structures (particles or droplets, blue circle in Figure

9 b). The height of the particle are in a range of 80 nm. After the reaction the surface was rinsed with ethanol and water to remove by-products and not-reacted compounds. No obvious difference of the surface was observed before and after reaction and cleaning (red circles in Figure 9, a) and c)), especially the *RMS* roughness was of the same order ( $0.5 \pm 0.1$  nm). Thereby, an influence by fluorination to the surface roughness can be neglected.

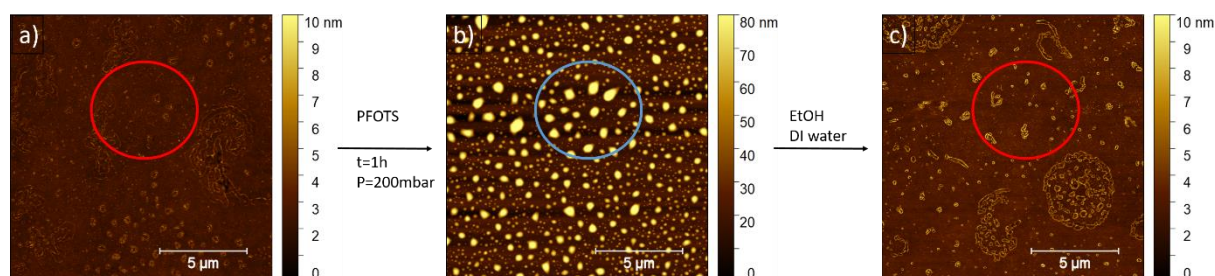


Figure 9: The fluorination was analyzed by AFM. The surface of the slide was detected after slide pre-preparation and before fluorination (a)). After one hour fluorination the slide was taken out of the desiccator and measured again (b)). Here an influence of fluorination to the surface is visible, some particle-like structures are visible. These structures could be by-products or non-reacted components of the reaction. After rinsing the surface with ethanol and DI water no by-products are observed at the fluorinated surface and further analysis showed a probably monomolecular layer of PFOTS on the slide (c)).

### 3.3.3 Silica particles

Silica particle were synthesized according to the Stöber reaction.<sup>[50]</sup> Ethanol was used as a reaction medium. Tetraethylorthosilicat (**TEOS**, 98%, Sigma-Aldrich,) was used as silane in the reaction. Ammonia solution (28%, VWR) was added as a catalyst. The particle size was controlled by the ratio between ammonia solution and TEOS.<sup>[50]</sup>

Ethanol (400 mL) was added to a glass sampling bottle (500 mL). While stirring (800 rpm), first TEOS and then the ammonia solution was added. After the start of the reaction no further turbidity was observed here after 2 hours. The solution was stirred for 11 h at room temperature.

In this work two different batches of silica particles were synthesized differing in size. To determine the particle size, the samples were measured with scanning electron microscope (**SEM**) and the particle size were calculated with the help of the software *ImageJ* (Figure 27). 60 particle were measured to calculate the average of the particle size. The error of the size was obtained by standard deviation. The respective particle concentration was determined gravimetrically. The volumes of chemicals and particle sizes are summarized in Table 2.

Cleaned slides (cf. chapter sample pre-preparation) were coated with particles as follows. The slides were placed in a petri dish (glass, d=10 cm, h=1.5 cm) and covered with the particle solution (V=5 mL). The solvent ethanol was evaporated at 50 °C. The coated slides were then baked for 20 hours in the oven at 60 °C to finish the crosslinking between the particles and the surface. The bonds between the silanes are formed by water elimination (chapter 2.4 Silanization/Fluorination). For coating with both



particle sizes, 5 mL of each solution was taken and combined. The solution was carefully stirred and then 5 mL was taken for coating.

After the coating the samples were fluorinated (chapter 3.3.2 Fluorination).

*Table 2: Approach of the synthesis of silica particle. Also listed are the determined particle sizes and the concentration of the solution. The error  $\Delta d$  is the standard deviation. The error of the concentration represents the error of the scale*

Particle	V(EtOH) / mL	V(NH <sub>3</sub> ,28%) / mL	V(TEOS) / mL	D / nm	$\Delta D$ / nm	c / mg mL <sup>-1</sup>	$\Delta c$ / mg mL <sup>-1</sup>
Particle A	400	25	14.5	108	±19	7.8	±0.1
Particle B	400	37.5	14.5	399	±28	9.1	±0.1

### 3.4 Etching

Before etching the slides were cleaned with ethanol (chapter 3.3.1 Sample pre-preparation). The slides were etched with a potassium hydroxide (**KOH**) solution. To investigate the effect of etching on the slides, the slides were placed in chromatography boxes containing solutions with different pH-values (12, 14). The etching time was also varied. A period of two and seven days was for each pH value selected. The parameters of the approaches are recorded in Table 3.

*Table 3: Approach of the etching series. The slides were etched in KOH solutions. The error of the weighted-in quantity corresponds to the error of the scale and the error of the volume corresponds to the error of the glass device.*

pH	m(KOH) / g	$\Delta m(\text{KOH})$ / g	V(H <sub>2</sub> O) / mL	$\Delta V(\text{H}_2\text{O})$ / mL
12	0.14	±0.01	250	±1
14	14.03	±0.01	250	±1

### 3.5 Sandblasting

The slides were sandblasted by the mechanical workshop of the Max –Planck –Institute for Polymer Research (**MPiP**, Mainz, Germany). The sand (SiO<sub>2</sub>) used had a grain size of 100-200 µm (AUER, Mannheim, Germany). The slides were treated with a pressure of 1.5 bar or 2.0 bar. With a smaller pressure the surface roughness could not be changed considerably. With a higher pressure the surface roughness was beyond the spatial resolution of the *AFM* and thus is unsuitable for this master thesis.

### 3.6 Sandpaper

The surface roughness of the slides was changed with silicon carbide (**SiC**) sandpaper. Here, a series of experiments were carried out with different grit sizes of sandpaper ( $P80 \triangleq 201 \times 10^3 \text{ nm}$ ,  $P280 \triangleq 52 \times 10^3 \text{ nm}$ ,  $P800 \triangleq 22 \times 10^3 \text{ nm}$ ,  $P1500 \triangleq 13 \times 10^3 \text{ nm}$ ). As the P-numbers increase, the grit size of the sandpaper decreases.

In order to work with a possible reproducible grinding method, the following procedure was used. A sandpaper was attached to a grinding block. This grinding block (Figure 10, b) was made by the mechanical workshop of the MPIP. Weights were placed onto the grinding block. The total weight was 692 g and the area was  $12.5 \text{ g/cm}^2$ . To protect the corners and edges of the slide during grinding four additional slides were added (Figure 10, a). In order not to exert any additional force, the block was pulled over the surface with the help of a string. The slides were grinded for 5 minutes each in the x and y direction respectively. Figure 10 shows the experimental set up.

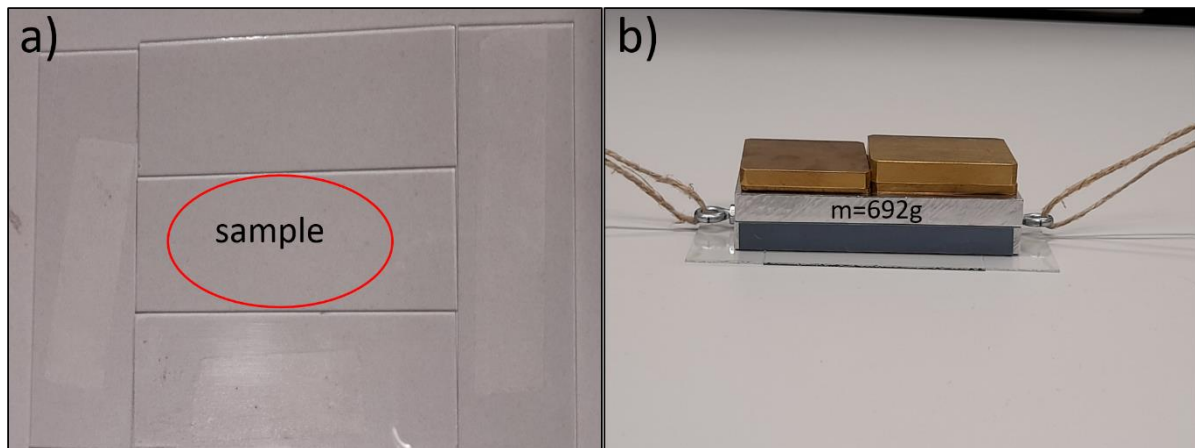


*Figure 10: Experimental setup of the experiment “grinding with sandpaper”. During the first experiments it was observed that the edges of the slides were stronger grinded than the rest of the surface or the slide was even broken. To protect the edges four slides were added around the sample (a)). Then the surface was grinding by pulling the grinding block with the cord (b)).*

### 3.7 Measurement RMS roughness

The measurements of the surface roughness were done either with *AFM* or *profilometer*. *AFM* measurements in tapping mode were performed on the *JPK Nanowizard 4* (Bruker Nano GmbH, Massachusetts, USA). Measurements were done with the cantilever type *OPUS, 160AC-NA*, 300 kHz, 26 N/m, typical tip size (radius)  $\leq 7 \text{ nm}$ , back side coating with reflective aluminum. Scan size were  $15 \times 15 \text{ }\mu\text{m}$  (no difference of surface roughness was detected at a scan size of  $1 \times 1 \text{ }\mu\text{m}$ ). All images were created with the help of the software *Gwyddion 2.59*. To calculate the *RMS* roughness the images were flattened using a polynomial of first degree. Each sample was measured at least two times. The error was determined using standard deviation.

Measurements with a scan length of 500  $\mu\text{m}$  were done with the *profilometer KLA-Tencor P7* (KLA, California, USA). The measurements were done with a scan speed of 10  $\mu\text{ms}^{-1}$ , sampling rate of 100 Hz and an applied force of 0.5 mg. Each sample was measured at least two times. In the further text the scan size is given in  $\mu$ .  $\mu$  corresponds to  $\mu\text{m}$ .

### 3.8 Charge measurement

A custom made experimental setup was used for the charge experiments.<sup>[15]</sup> Figure 11 shows a photo of the experimental setup and Figure 12 shows a schematic illustration of the setup. The whole setup is placed in a Faraday cage (1) to protect from external electromagnetic fields and every metal component is grounded. Sample are fixed at the aluminum plate (2) and with the help of the rotatable holder (3) the tilt angle can be adjusted. A metallic needle (4; inner diameter 2 mm) is connected to a peristaltic pump (Gilson, MINIPULS 3, Wisconsin, USA) with a tube. The drop height as well as speed of the pump can be varied. After leaving the needle the drop is grounded by touching a wire, which is fixed at the holder. A laser beam (source: laser pointer (5)) is reflected from the surface and is detected by a photodiode (6). As the laser path is blocked by the sliding drops, a voltage reduction at the photodiode is detected. An edge of this voltage drop is used to count the drops and to start the measurement. A probe (7) connected to a current amplify (8) (DDPCA-300, Femto, Germany) is used to discharge the sliding drops and measure the discharge current. Here the electrical resistance of  $10^6 \Omega$  is chosen. Data acquisition is done using a multifunction box (National instruments, NI USB-6366, Hungary) connected to a computer. The drops were collected in a vessel (9). An Ionic air blower (10) (Simco-Ion, Aerostat PC Ionizing Air Blower, Pennsylvania, USA) is installed to electrically neutralized the surface of the sample before charge measurement.

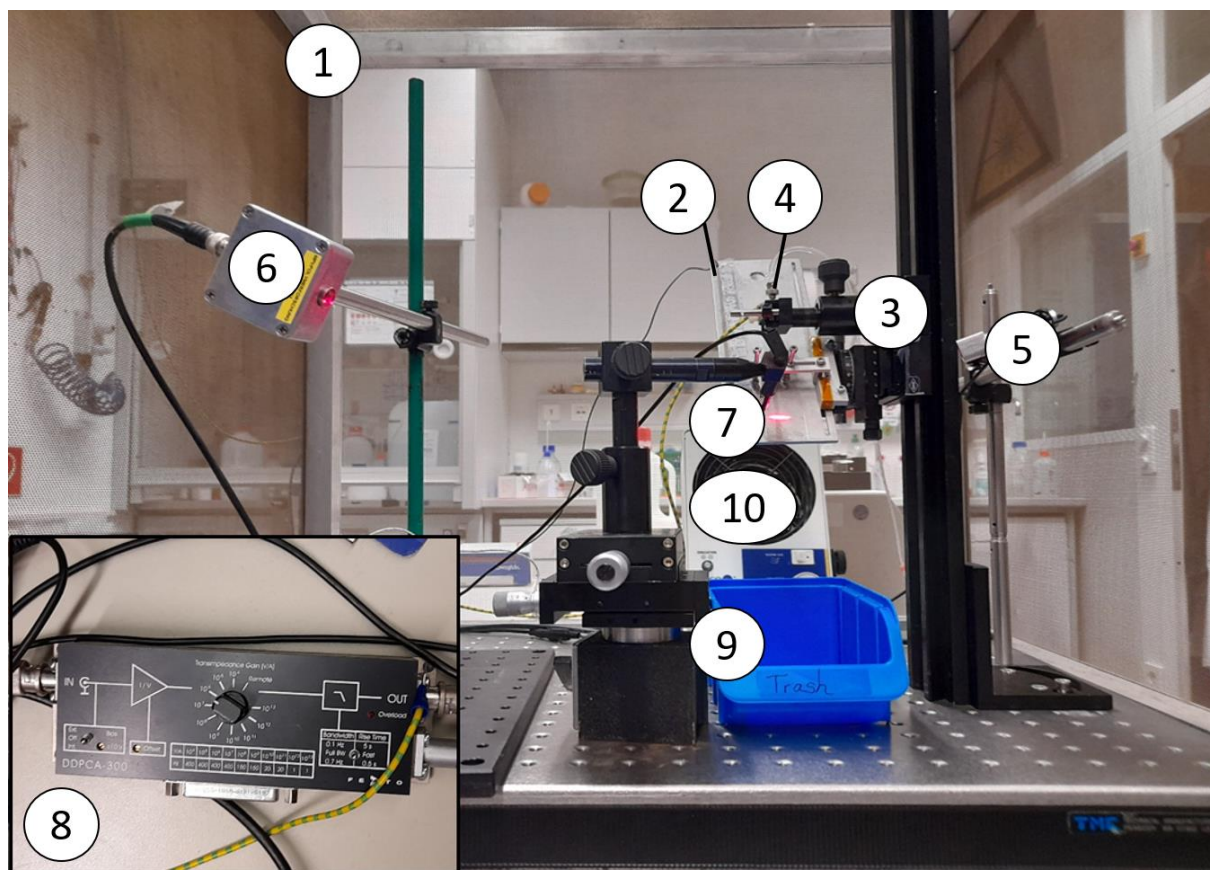


Figure 11: Experimental setup of charge measurement. (1) Faraday cage. (2) Aluminum plate. (3) Rotatable holder. (4) Needle. (5) Laser pointer. (6) Photodiode. (7) Sample and sample holder. (8) Current amplifier. (9) Vessel. (10) Ionic air blower.

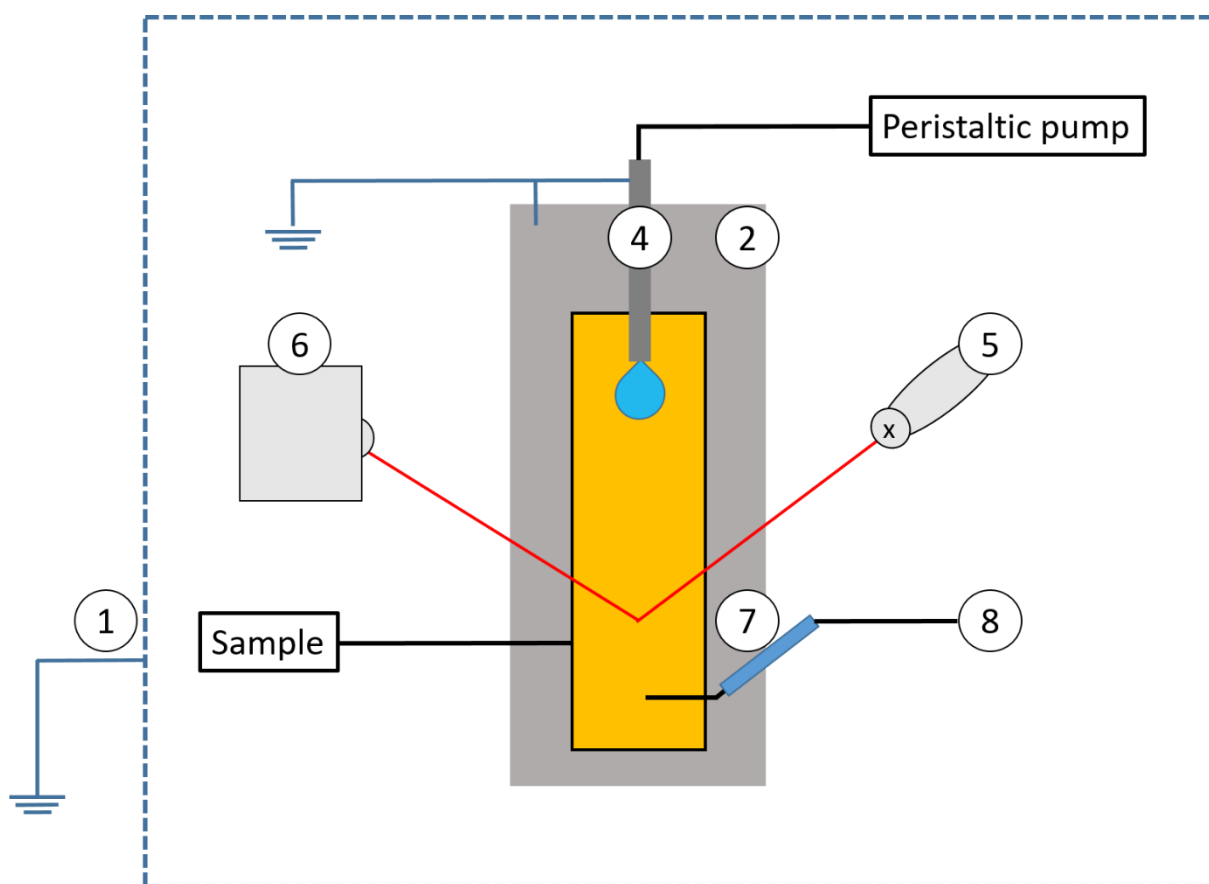


Figure 12: Schematic drawing of the charge measurement setup. For a better overview the scheme is given from a top view. All metal parts are grounded and connect to the Faraday cage (1). The sample is fixed on the sample holder (2). The sample holder can be rotated to adjust the tilt angle (3, not shown here). The needle (4) is connected to a peristaltic pump. The drop height as well the speed of the pump can varied. With the laser (5) a voltage can be measured by the photodiode (6) by reflection of the laser beam at the surface of the sample. The electrode (7) is connected to a current amplifier to detect the charge of the sliding drop.

Each sample was measured with 500 successive drops three times at three different places on the sample. Before each measurement, the surface was neutralized for 5 minutes with the ionizing air blower. The measurement was done with a tilt angle of 50°. A fixed slide distance of 4 cm was used for the measurement. The drop rate was regulated with the peristaltic pump and the time between successive drops was 2 s. Drop size was  $45 \pm 2 \mu\text{L}$ . Fall height of the drops was 0.5 cm. Fresh DI water ( $18.2 \text{ M}\Omega\text{cm}$ ) was used for each experiment. The data analysis was done with the help of the software *Python 3.8 spyder (Anaconda 3)*, *Origin 2021* and *Microsoft Excel 2016*.

### 3.9 Contact angle goniometer

Static-, advancing- and receding contact angle (**SCA**, **ACA**, **RCA** respectively) were measured by *OCA35* device (DataPhysics Instrument GmbH, Germany). Figure 14 shows the experimental setup. The

sample is placed on the sample holder (2). Video recording and analysis were done with the camera (4) and with the help of the software *SCA20 provided by DataPhysics Instrument GmbH*. A 'warm white' LED (3000 K) is used as light source for the measurement (3). A water drop (6  $\mu\text{L}$ ) is placed with a *Hamilton* syringe ((1) 100  $\mu\text{L}$ , needle: blunt end, coated with *PTFE* to make it hydrophobic, 51 mm length, inner diameter: 0.4 mm) on the surface. After setting the baseline, *SCA* was measured. For the measurement of the *ACA* and *RCA* the volume of drop was increased and decreased by 40 or 50  $\mu\text{L}$  (depend on the surface) with a rate of 0.5  $\mu\text{Ls}^{-1}$  and 2 repeats. Each sample was measured two times at different places on the sample and the average was used for the evaluation. Error was calculated by standard deviation. To calculate *ACA* and *RCA* the recorded video was analyzed. The *CA* was calculated by a circle fit. For the *ACA* the average value of the recorded plateau was used (blue circles in Figure 13). The determination of the *RCA* could not be done with the help of the plot because no plateau but only a minimum was observed for the *RCA* (red circle in Figure 13). The *RCA* was determined visually. In accordance to the theory of advancing and receding contact angle the angle at which the three-phase contact line starts to move was noted for the receding contact angle.<sup>[24]</sup>

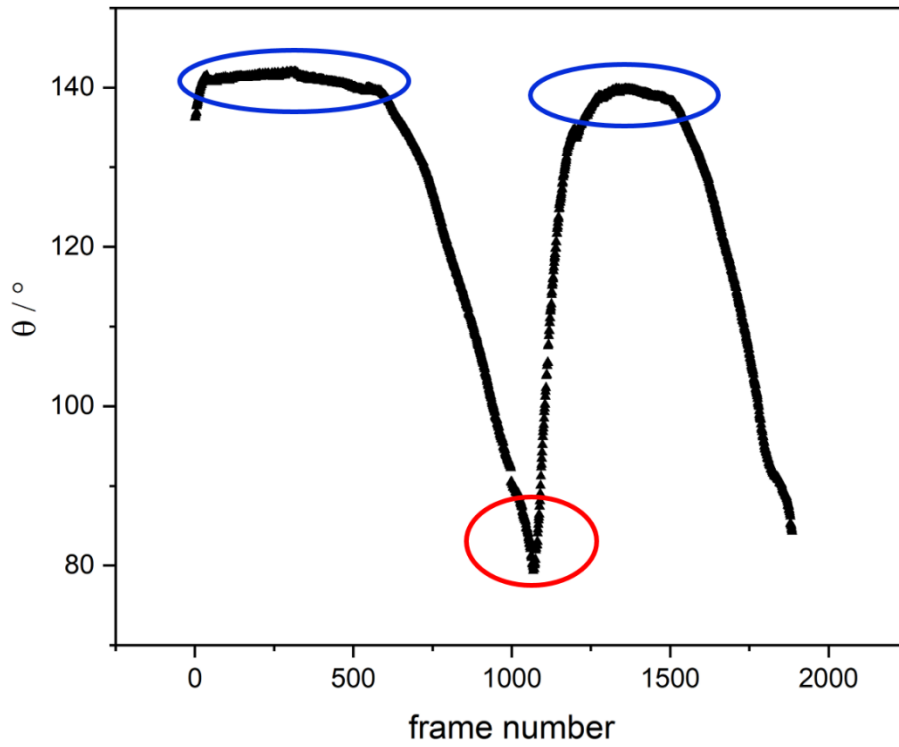


Figure 13: Advancing (ACA) and receding (RCA) contact angle of a water drop on a fluorinated N-LASF45 glass slide. Plot of the contact angle against the frame number. After the drop is placed on the surface, the drop volume is increased from 6 to 50  $\mu\text{L}$ . Then the drop volume is reduced again to 6  $\mu\text{L}$  and the process is repeated again. The contact angle of the drop is recorded by a circle fit during the measurement. During increase of the drop volume, the contact angle reaches a maximum (blue circles). This angle is the ACA. The ACA was calculated by averaging the two plateaus (blue plateaus). In contrast to the ACA, the RCA cannot be determined using a plateau in the plot. The minimum of the plot does not correspond to the definition of the RCA (red circle). The RCA is determined as the point when the drop moves visually.<sup>[24]</sup>



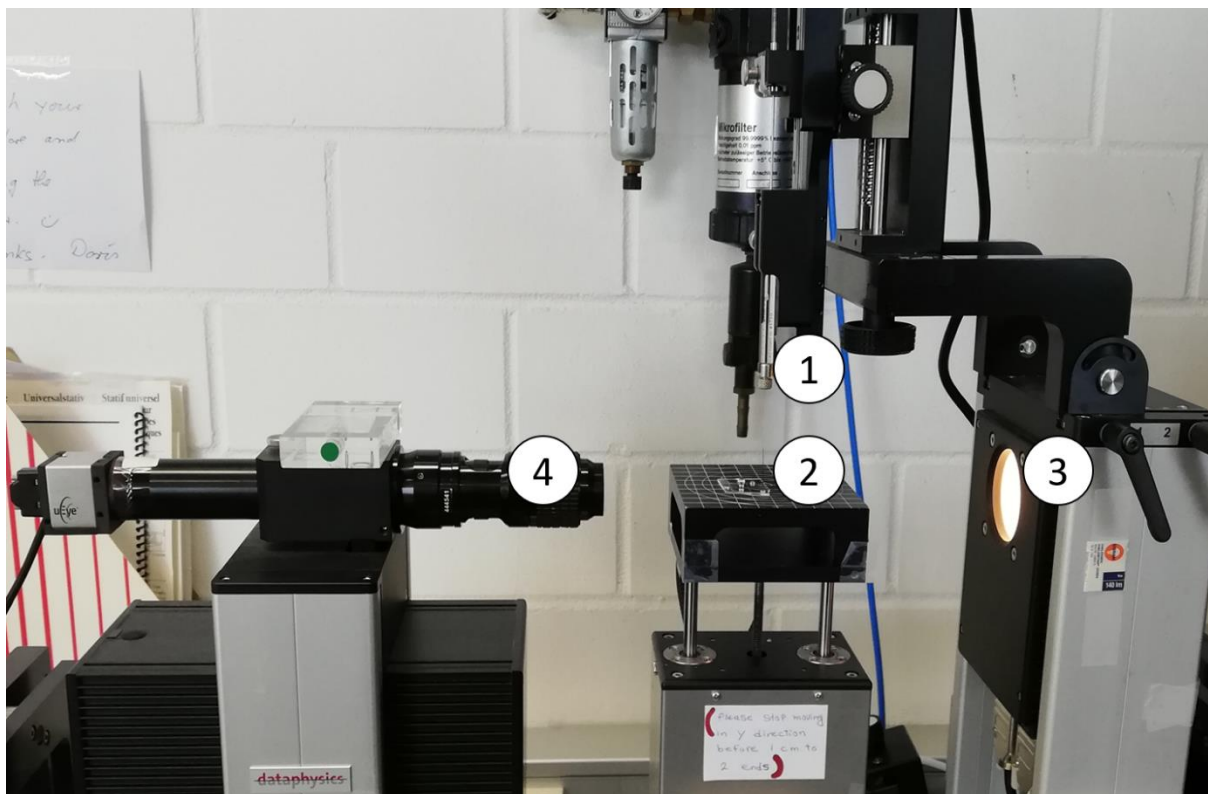


Figure 14: Goniometer DataPhysics OCA35. (1) 100  $\mu\text{L}$  Hamilton syringe with needle. (2) Sample and sample holder. The sample holder can be moved with a motor in x,y,z. (3) A Lamp as light source to record and calculated the contact angle with the camera (4). The whole goniometer can be tilted to record roll off angles.

### 3.10 Scanning electron microscope

Scanning electron microscope measurements were done with a *LEO 1530 GEMINI* / Carl Zeiss Microscopy Deutschland GmbH, construction year 1998, EHT=100 V-30 kV.

### 3.11 Velocity measurements

A custom made experimental setup (MPIP, Figure 16) was used for the velocity measurements of the water droplets.<sup>[51]</sup> The drop is applied to the surface via the needle (3; inner diameter 1 mm), its height can be adjusted. The syringe is connected to a peristaltic pump (Gilson, MINIPULS 3, Wisconsin, USA). The speed of the pump can be varied to control the time between droplets. All metal components are grounded. The setup is fixed on a plate which can be rotated (1). Thus, the tilt angle can be changed. When the drop slides down the sample, it is recorded by a high speed camera (Photron, Fastcam Mini UX10). Using the software *Matlab*, a polynomial fit of fourth degree is placed over the moving droplet. The modified *Matlab* code<sup>[52]</sup> is based on the work of Andersen et al.<sup>[53]</sup> The polynomial fit is shown schematically in Figure 15. The fit is used to calculate the velocity, advancing and receding contact angle.



In this work a tilt angle of 60 degree was used. This tilt angle was used because in a case of a lower tilt angle (50 degree) the drop does not move. The drop volume was  $30 \pm 2 \mu\text{L}$ . The velocity was determined over a length of 4 cm. The average value of recorded front and back speed of the water drop was taken to calculate the velocity. 100 drops were measured for the evaluation. The first 100 drops were not measured. During the first 100 drops sometimes two drops were recorded by the camera. Therefore the fitting was manipulated and the data cannot be used for evaluation.

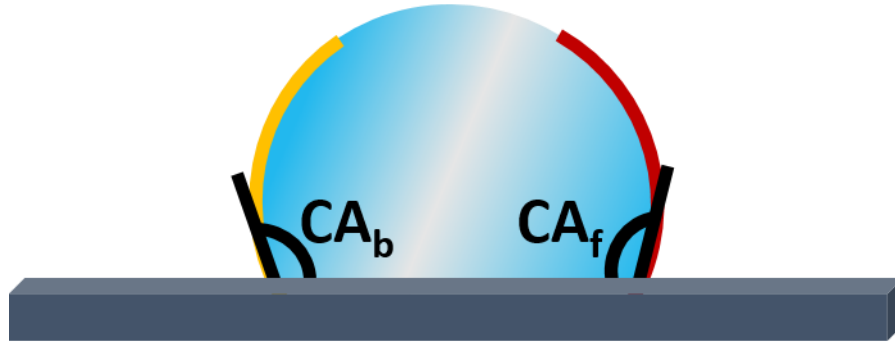


Figure 15: Schematically illustration of the applied polynomial fit during the velocity measurement. After recording the sliding drop by the high speed camera the drop is evaluated with the polynomial fit of fourth degree. A fit is placed over both the drop front (red line) and the drop back side (orange line) of each recording. The contact angle (CA) of the drop front ( $CA_f$ ) and the drop back side ( $CA_b$ ) is calculated. The  $CA_f$  is the advancing contact angle during movement. The  $CA_b$  is the receding contact angle during movement. The velocity from the drop front and drop back side is also calculated by the polynomial fit.

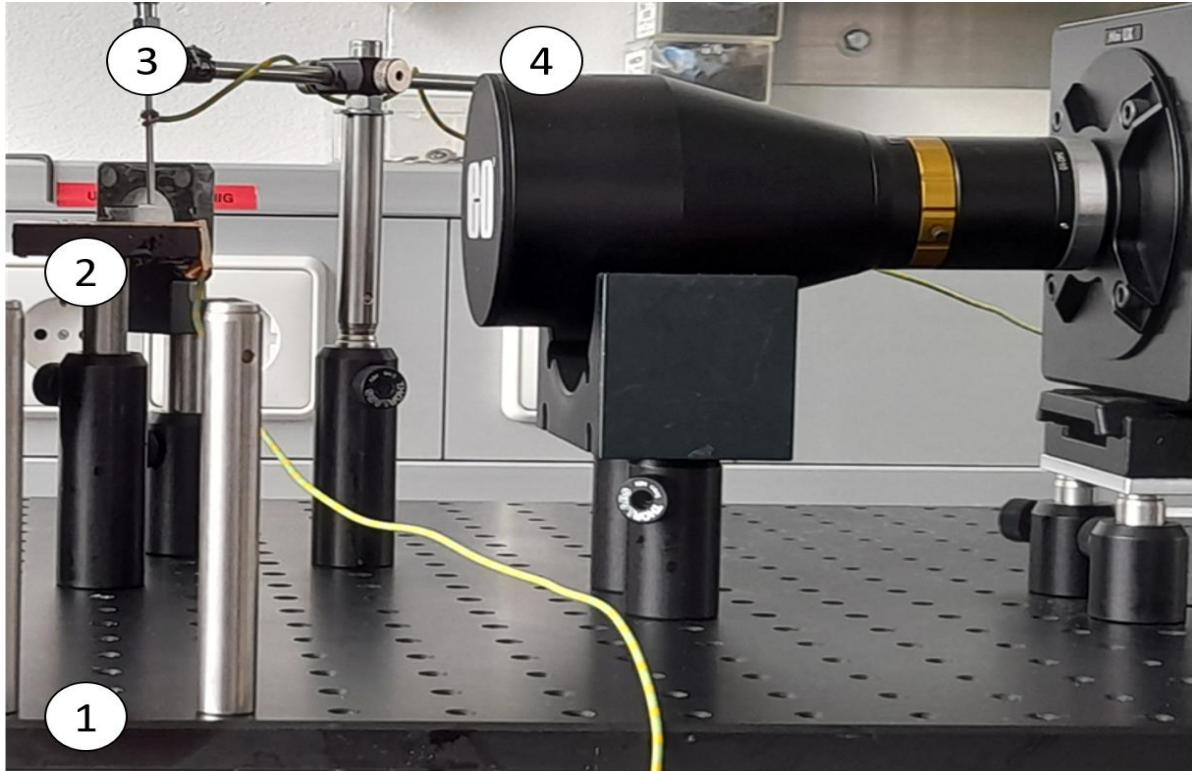


Figure 16: Experimental setup of the velocity measurement of the water drops. (1) Experimental setup is fixed at a plate that can be rotated to change the tilt angle. (2) Sample holder. (3) Syringe. (4) High speed camera.

## Chapter IV: Results and discussion

For a better overview this section is divided into sections. First the methods to change the surface roughness second the results of the charge measurements. This is followed by a discussion and presentation of the final results of this work.

### [4.1 Changing surface roughness](#)

The surface roughness of the microscope slides (in the following called **slides**) was changed by etching, sandblasting, grinding with silicon carbide sandpaper and coating with silica particle.

#### 4.1.1 Etching

The slides were etched with *KOH* solution under different conditions (chapter 3.4 Etching). The results are summarized in Figure 17.

A comparison of the *AFM* images and the *RMS* roughness show that the influence of etching is very small. The chemical resistance of glass to acids and bases is well known.<sup>[40, 48]</sup> Nevertheless, a bigger influence from etching was expected here, but not found in this master thesis.<sup>[54]</sup> The *AFM* images (Figure 17) show the typical surface structure of the slides in all experiments (blue circles in Figure 17: a), c), e)). In some surface areas a change of the surface could be observed (red circle in Figure 17: d)). This indicates that the etching process is slowly starting here. Possibly a greater influence of etching could be observed with a longer etching time or etching with hydrofluoric acid.<sup>[55]</sup>

All in all, **no obvious change** in the *RMS* roughness within the error of the experiment was determined here.

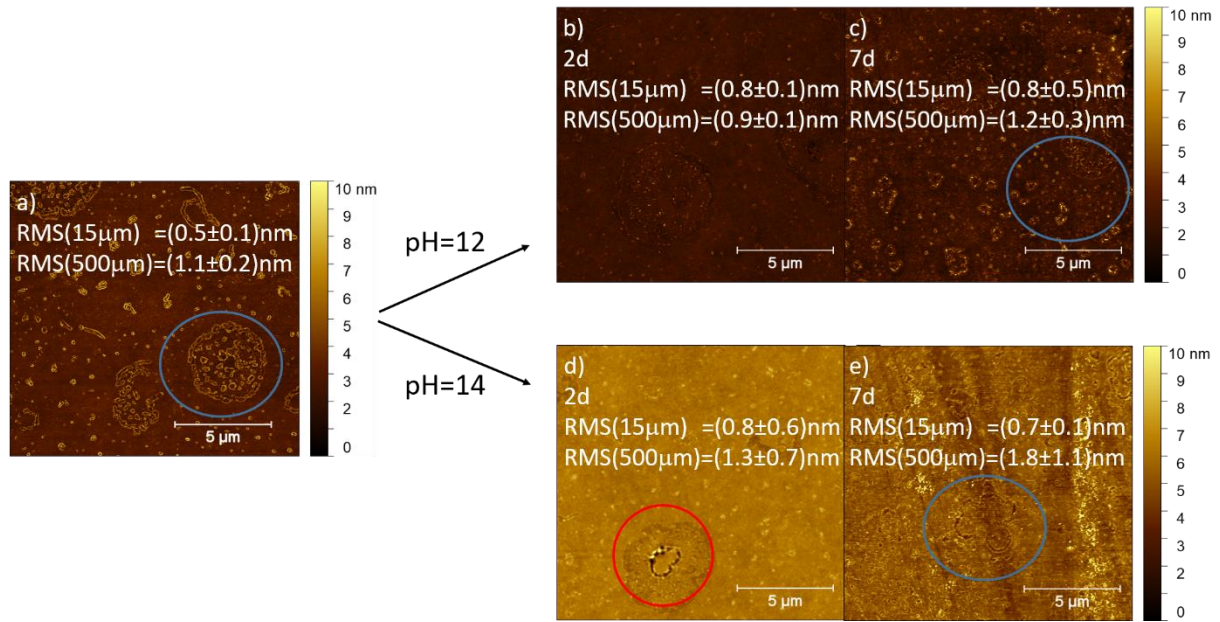


Figure 17: Influence of etching with KOH on the surface roughness of the slide under different conditions. Images were recorded with the AFM. The RMS roughness were calculated at a scan size of 15 μ (AFM) and 500 μ (profilometer). a) Pristine fluorinated slide, b) etched slide at pH 12 and 2 days etching time, c) etched slide at pH 12 and 7 days etching time, d) etched slide at pH 14 and 2 days etching time, e) etched slide at pH 14 and 7 days etching time. All images show the surface structures of a pristine slide (blue circles). That means the influence of etching with KOH is small. This is also evident from the calculated RMS values.

#### 4.1.2 Sandblasting

By means of sandblasting (chapter 3.5 Sandblasting), the surface roughness could be changed. The AFM images of the sandblasted surfaces are shown in Figure 18. In contrast to the slide surface (blue circles in Figure 17), there are no longer any typical slide structures to be seen. Particularly in the case of sandblasting at 2 bar, the RMS roughness increases significantly. Here a transition from nanoscopic ( $RMS$  roughness < 100 nm) to macroscopic surface roughness can be observed.<sup>[56]</sup> The high RMS error values represent that inhomogeneous rough surfaces were produced. In all measurements no sand grains or residues from sandblasting are seen. It can be assumed that the surface chemistry was not change here.

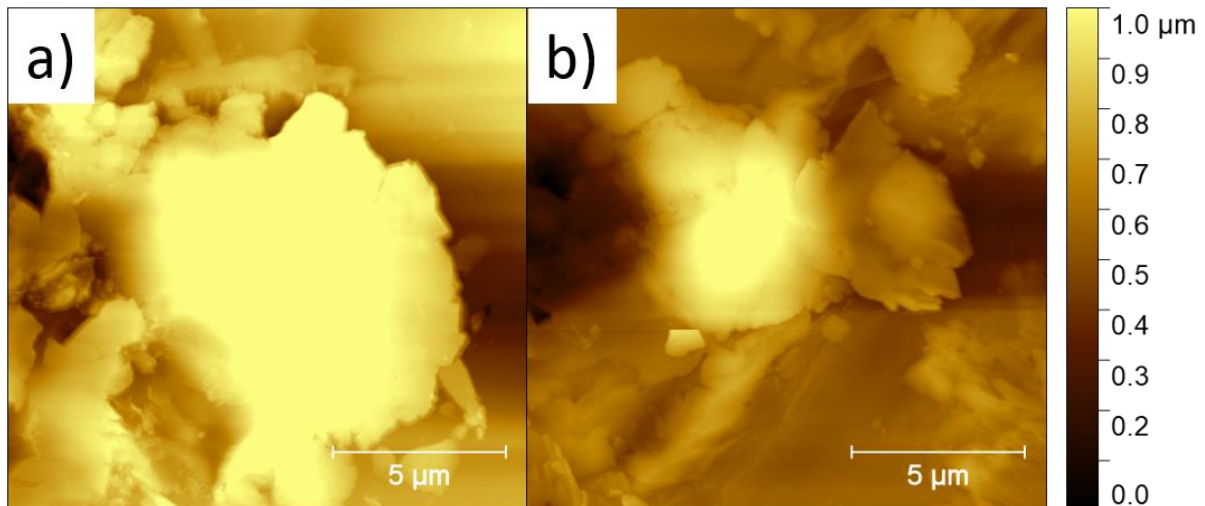


Figure 18: AFM images and calculated RMS roughness of the sandblasted slides at different pressure. a) Sandblasted at 1.5 bar,  $RMS(500\mu)=(104\pm71)$  nm,  $RMS(15\mu)=(9\pm6)$  nm. b) Sandblasted at 2.0 bar,  $RMS(500\mu)=(498\pm315)$  nm,  $RMS(15\mu)=(105\pm39)$  nm. In both experiments the surface changed visibly. The surface roughness increased with the pressure of the sandblasting. The errors show that by sandblasting the surface roughness is changed inhomogeneous.

#### 4.1.3 SiC-sandpaper

The surface of the slides was treated with different types of sandpaper (chapter 3.6 Sandpaper) AFM images and calculated RMS values are summarized in Figure 19. In all experiments a change of the surface roughness could be observed. The AFM images show that grinding with a higher grit size leads to deeper grooves (red circles in Figure 19, a), c) d)). There were a lot of areas on the surface where the surface roughness did not change (blue circle in Figure 19, b)). These measuring points are the area between the grinding grooves. It could be observed that the distance between the grooves increase with increasing grit size. E.g. when using P80 sandpaper it could be observed that the grooves were far apart. Especially in the AFM, either untreated areas or grooves could be measured. No residues from the sandpaper were observed. A change in the surface chemistry can therefore be neglected.



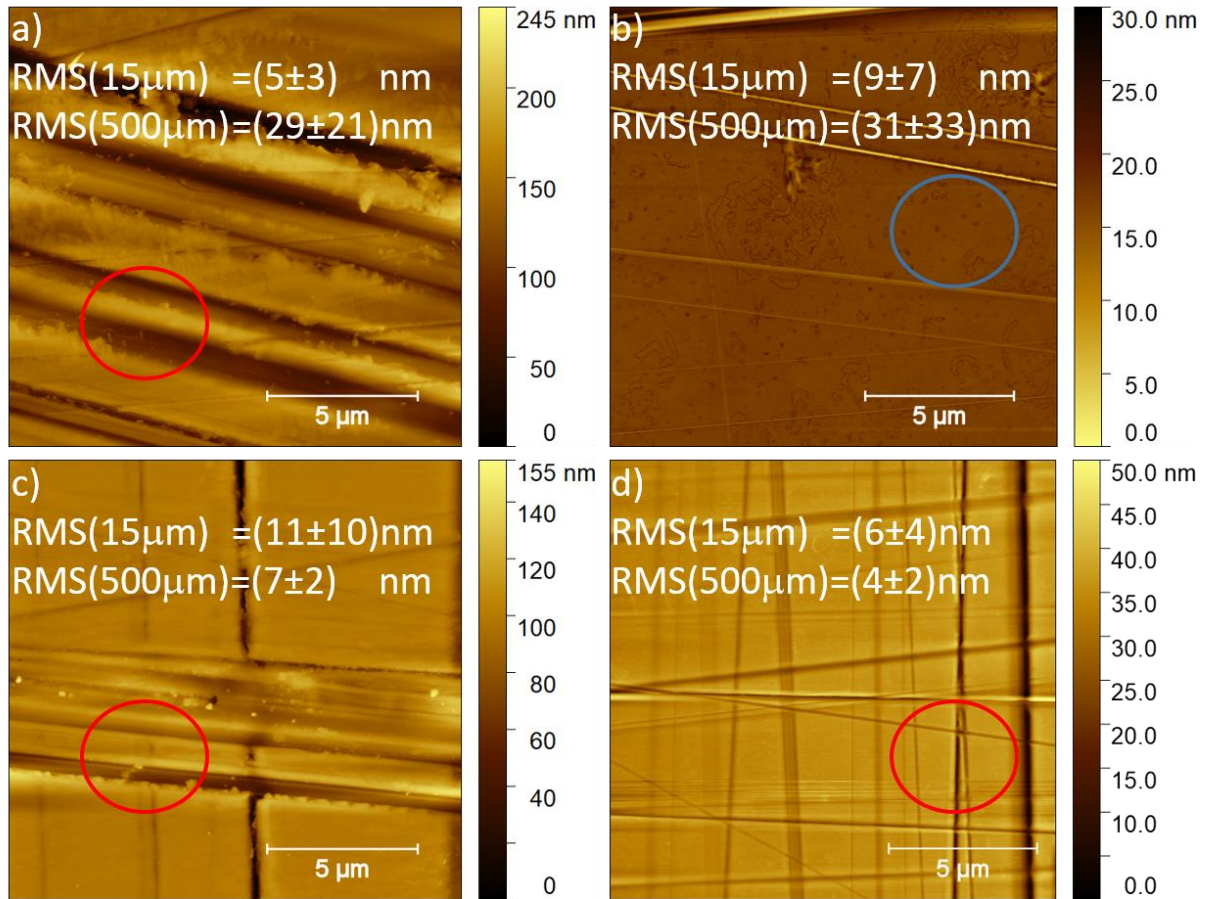


Figure 19: AFM images and calculated RMS values of the slides after grinding with different SiC sandpaper: a) Label P80, grit size 221  $\mu\text{m}$  b) P280, grit size 52  $\mu\text{m}$  c) P800, grit size 22  $\mu\text{m}$  d) P1500, grit size 13  $\mu\text{m}$ . In all AFM images grooves are visible. The distance between the grooves is dependent on the used size of SiC particle at the sandpaper (red circles). There are areas of the surface where the influence of the grinding is small. In this areas the typical surface structures of a pristine slide are visible (blue circle).

#### 4.1.4 Coating with silica particle

Coating the slides with silica particles is a method to manipulate the surface roughness enormously (chapter 3.3 ). AFM images of the coated slides are collected in Figure 20. The changing of the surface roughness can be controlled by the particle size and their distribution (Figure 20; a), b), d)). The inhomogeneity of the surfaces resulted in a large error of the RMS values. By coating with the silica particles, not only the surface roughness but also the surface chemistry was changed.

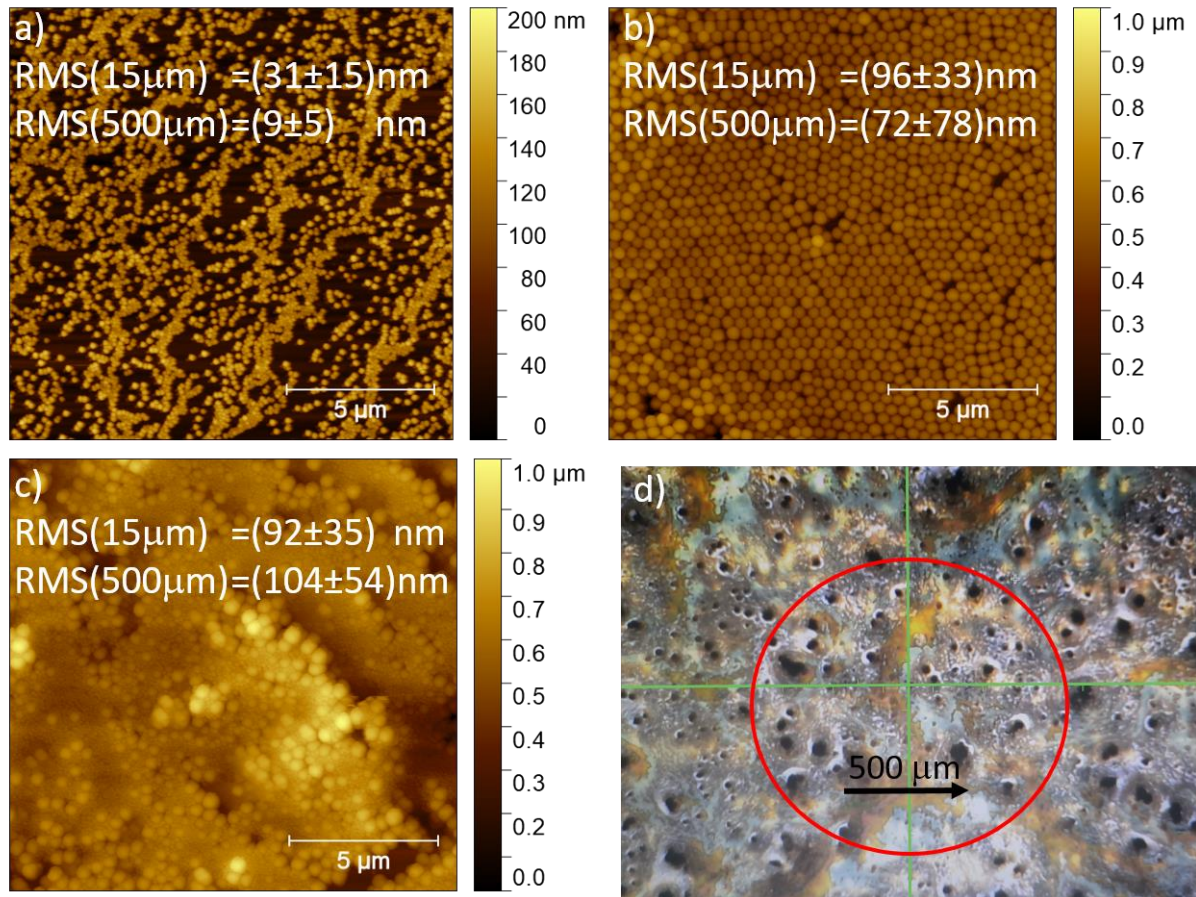


Figure 20: a) AFM image and calculated RMS values of the slide coated with silica particle (particle size: 108 nm). Between the silica particles vacancies are visible b) AFM image and calculated RMS values of the slide coated with silica particle (particle size: 399 nm). There are almost no vacancies and the particles are piling up. c) AFM image and calculated RMS values of the slide coated with silica particle (mixed particle size). Multiple layers of particles are visible. d) Camera picture of a sample coated with silica particle. The picture was taken with the camera of the profilometer. With the crosshair the measuring point can be chosen. The black arrow illustrates the scan size of 500 μ. It is obvious that the surface roughness depends on the measurement point.

#### 4.1.5 Results and discussion of the calculated RMS roughness

All calculated RMS values are summarized in Table 4. On the one hand the large error shows on the one hand the statistical character of the RMS roughness (chapter 2.1 Surface roughness) and on the other hand the inhomogeneity of the surfaces. Especially for inhomogeneous surfaces such as those obtained by sandblasting or grinding, the calculation of the RMS values is not so clear and shall be discussed briefly here. If the chosen scan size used is too small, no or only a small difference of the surface roughness can be measured between different samples. For example the analysis of the surface, which was coated with silica particle or grinded with sandpaper. Here, either untreated surface areas or treated surface areas were measured with the AFM. To prevent this, a larger scan size can be used for measurement. In the case of very inhomogeneous surfaces the *profilometer* is the better method to detect the surface roughness. For flat and homogeneous surfaces such as the glass

substrates, the *AFM* is the optimal technique to calculate the surface roughness. Therefore, the scan size with which the *RMS* values were determined is always specified in the further discussion.

*Table 4: Calculated surface roughness (RMS) of all samples. The RMS roughness was calculated at a scan size of 15 x 15  $\mu\text{m}$  with the AFM and 500  $\mu\text{m}$  with the profilometer. The error was calculated by standard division.*

Sample		<i>RMS</i> (15x15)	$\Delta$ <i>RMS</i> (15x15)	<i>RMS</i> (500)	$\Delta$ <i>RMS</i> (500)
		/ nm	/ nm	/ nm	/ nm
Fluorinated slide		0.5	$\pm 0.1$	1.1	$\pm 0.2$
Etching	pH12, 2d	0.8	$\pm 0.1$	0.9	$\pm 0.1$
	pH12, 7d	0.8	$\pm 0.5$	1.3	$\pm 0.3$
	pH14, 2d	0.8	$\pm 0.6$	1.3	$\pm 0.7$
	pH14, 7d	0.7	$\pm 0.1$	1.8	$\pm 1$
Sandblasting	1.5 bar	9	$\pm 6$	104	$\pm 70$
	2.0 bar	104	$\pm 39$	499	$\pm 315$
Sandpaper	P80	5	$\pm 3$	29	$\pm 21$
	P280	9	$\pm 7$	31	$\pm 33$
	P800	11	$\pm 10$	7	$\pm 2$
	P1500	6	$\pm 4$	4	$\pm 2$
Silica particle	Particle A	31	$\pm 15$	9	$\pm 5$
	Particle B	96	$\pm 33$	72	$\pm 78$
	Particle A+B	92	$\pm 35$	109	$\pm 54$
Quartz glass		0.5	$\pm 0.1$	0.8	$\pm 0.1$
N-LASF45		0.7	$\pm 0.1$	0.6	$\pm 0.1$

## 4.2 Charge measurement

In this section the influence of the surface roughness on the charge measurements is discussed. For the comparison the drop charge (saturated) was used (chapter 3.8 Charge measurement). For a better overview some sample are not shown here. All samples whose surfaces have been etched are not included in the discussion, as the surfaces roughness have not been changed compared to the slides (chapter 4.1.1 Etching). Furthermore, the samples which were grinded with sandpaper (P80, P1500) are not shown in this section (cf. appendix Figure 28, Figure 29 and Figure 30).

To investigate the influence of surface roughness on the drop charge, the drop charge was first plotted against the drop number in consideration of the surface roughness. Then the saturated drop charge was plotted against the *RMS* roughness (blue dashed line in Figure 21 and Figure 22). The Figure 21 shows the results with a *RMS* roughness recorded at a scan size of 15  $\mu$  with *AFM*. When we compare the plots in Figure 21 (b)), we see that the drop charge decreases with increasing *RMS* roughness. We also see that two completely different samples have an *RMS* value of 9 nm (red and blue plot in Figure 21). Inhomogeneous surfaces were produced with both methods and as shown in the previous section, for this kind of surfaces the measurement of the surface roughness with a scan size of 15  $\mu$  might be too small to reflect the actual surface roughness (chapter 4.1.5 Results and discussion of the calculated *RMS* roughness ).



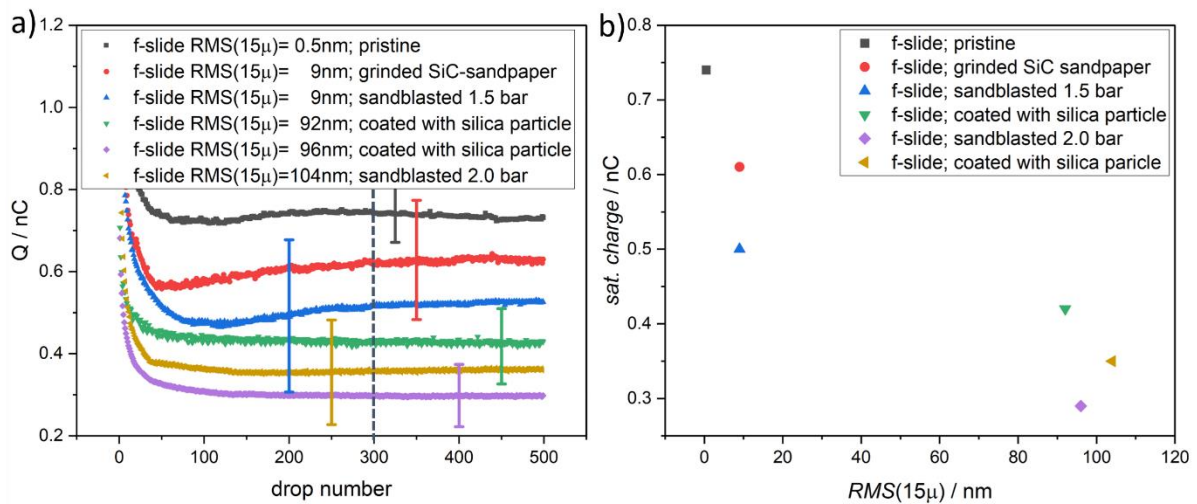


Figure 21: Results of the drop charge measurement in consideration of the surface roughness. The RMS roughness was calculated at a scan size of  $15\mu$ . a) Plot of the measured drop charge against the drop number. The dashed line represent the drop charge which was used for the saturated drop charge. b) Saturated drop charge against the RMS roughness. With increasing surface roughness the drop charge decreases. a) We see two different surfaces with a RMS roughness of 9 nm. The surface roughness of these both samples were changed by different methods (sandblasting and grinding with sandpaper). A comparison of the two surfaces with the naked eye showed that the surface roughness are different. It can be concluded that the scan size of  $15\mu$  used is too small and therefore the calculated RMS values do not reflect the actual surface roughness. The error bars correspond to the standard deviation.

To exclude the influence of a scan size that is too small, the results of the charge measurement are plotted again in Figure 22. Here the RMS roughness was calculated at a scan size of  $500\mu$  with the *profilometer*. We see that with increasing surface roughness the drop charge decreases. If we compare the plots in the range from 0 to 100 nm Figure 22 (b)), we see no clear tendency between the drop charge and surface roughness. The sample with the lowest and highest drop charge is in this range. The question here was, whether there is another parameter besides the surface roughness that influences the drop charge. To answer this question the methods used to change the surface roughness were compared (orange circles in Figure 22 b)). The samples where the surface roughness has been changed mechanically (chapter sandblasting, grinding with SiC-sandpaper), the chemical composition and surface chemistry should not have changed. It is different with the surfaces that were coated with silica particle. Both the surface roughness and surface chemistry were changed here.

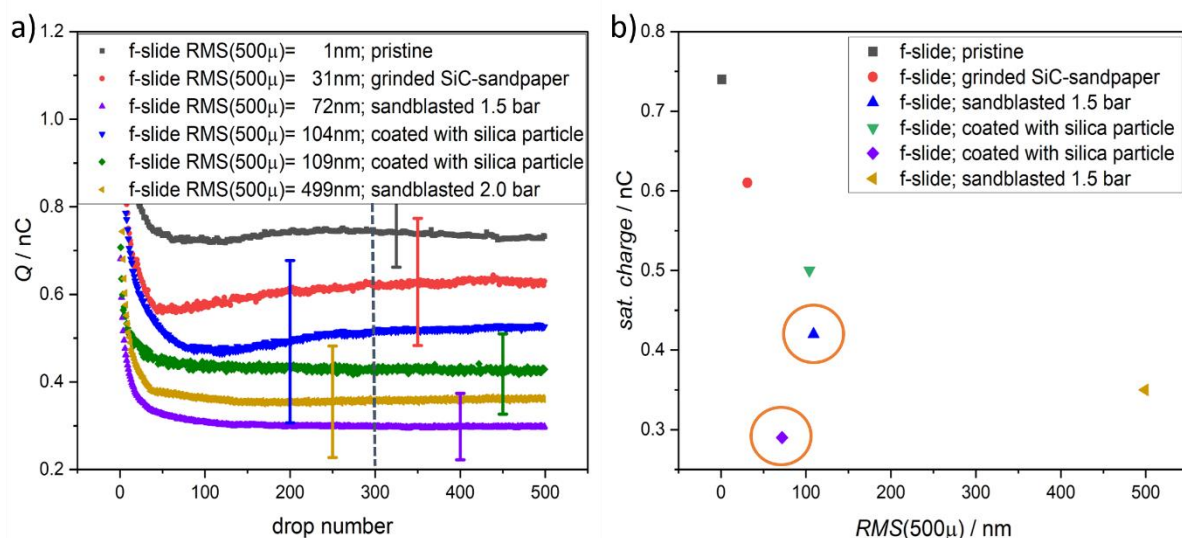


Figure 22: Results of the drop charge measurement in consideration of the surface roughness. The RMS roughness was calculated at a scan size of 500  $\mu$ . a) Plot of the measured drop charge against the drop number. The dashed line represents the drop charge which was used for the saturated drop charge. b) Plot of the saturated drop charge against the RMS roughness. On the one hand we see that the drop charge decrease with increasing surface roughness. On the other hand we find in the range from 0 to 100 nm the minimum and maximum of drop charge. To understand this, the method with which the surface roughness was changed were compared (orange circles in b)). It turned out that in the samples where the surface roughness was changed mechanically (non-coated with silica particle) the drop charge decrease with increasing RMS roughness. It is different with the samples that have been coated with silica particle. Both the surface roughness and surface chemistry was changed here. It seems that apart from the surface roughness the surface chemistry or the chemical composition of the substrate influences the drop charge. The error bars correspond to the standard deviation.

To investigate the relationship between surface chemistry and surface roughness, the saturated drop charge has been plotted against the surface roughness in Figure 23. The black data marks represent the f-slides with different surface roughness and same surface chemistry. The red data marks represent the sample which were coated with silica particle. The surface roughness and surface chemistry of these samples were changed. The RMS roughness of a scan size of 500  $\mu$  is used (see chapter 4.1.5 Results and discussion of the calculated RMS roughness).

A comparison of the results shows us in the case of the non-coated (with silica spheres) f-slides the following: **With increasing surface roughness the drop charge decrease.** The results for the coated sample are different. There is no clear relationship between the surface roughness and the drop charge.

If we compare the drop charge of the samples with similar surface roughness but different surface chemistry, we see that their drop charge are far apart from each other (orange circle in Figure 23). It can be concluded that the surface chemistry influences the drop charge at least as much as the surface roughness does.

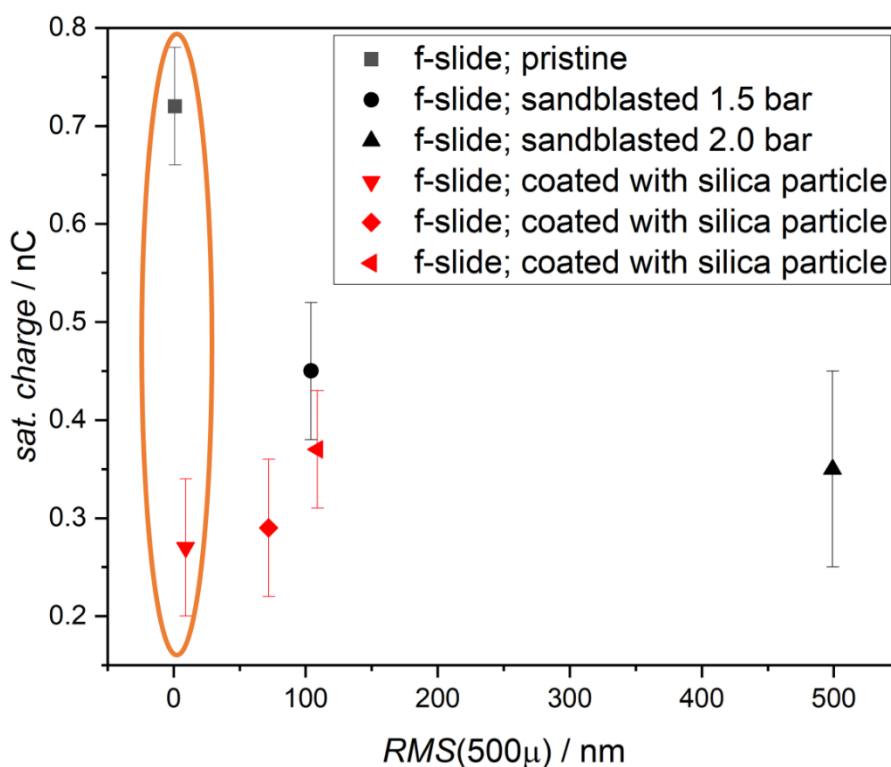


Figure 23: The saturated drop charge is plotted against the RMS roughness. The calculation of the RMS roughness was done at a scan size of 500  $\mu$ . To compare the influence of the surface roughness and the surface chemistry of the substrate on the drop charge, two different types of sample were used. The black data marks represent the f-slides as substrate with different surface roughness. The surface roughness was changed mechanically and so the surface chemistry of these samples should be similar. The red marks show the results of the f-slides which were coated with silica particle. Next to the surface roughness the surface chemistry of the substrate was changed here. If we compare the results separately we see the following: For the non-coated (silica particle) f-slides the drop charge decrease with increasing surface roughness (black marks). The red marks show no relationship between drop charge and surface roughness. Reason could be that the RMS roughness for inhomogeneous surfaces are not so clear. If we compare two samples with similar surface roughness but different surface chemistry we see the (orange circle) that the drop charge of these two samples is different. It can be assumed that next to the surface roughness the surface chemistry influence the drop charge.

In order to neglect the influence of inhomogeneous surfaces to the calculation of the RMS roughness, flat glass substrates with different chemical composition were used to check the influence of the surface chemistry to the drop charge. The RMS roughness was calculated at a scan size of 15  $\mu$  (chapter 4.1.5 Results and discussion of the calculated RMS roughness). The results are summarized in Figure 24. The saturated drop charge is plotted against the RMS roughness. Although the RMS roughness of the different glass substrates are in the same order of magnitude the saturated drop charge differ. The f-slides have the largest drop charge. The quartz glass slides show the lowest drop charge. This indicates that the ionic components of the substrate probably influence the drop charge. The question that remains open and could not be answered in the frame of this master thesis whether it is a specific ionic component or the mixture of components that affects the drop charge. The question arises

whether the dielectric constant of the glass substrate influence the drop charge. Since no dielectric constant could be measured in this master thesis, the refractive index (measured at  $\lambda=546$  nm) was used to compare the electric properties of the glass substrate. The comparison of the refractive index and the drop charge showed that there is no correlation between the drop charge and the dielectric constant of the substrate (Figure 24).

In conclusion, it can be stated here that the surface roughness has an influence on the drop charge. It was found that with increasing surface roughness the drop charge decrease. **It has been shown that besides the surface roughness, the surface chemistry of the substrate also influence the drop charge.** A comparison of the results (cf. Figure 23 and Figure 24) shows that the influence of the surface chemistry is larger than the influence of the surface roughness to the drop charge.

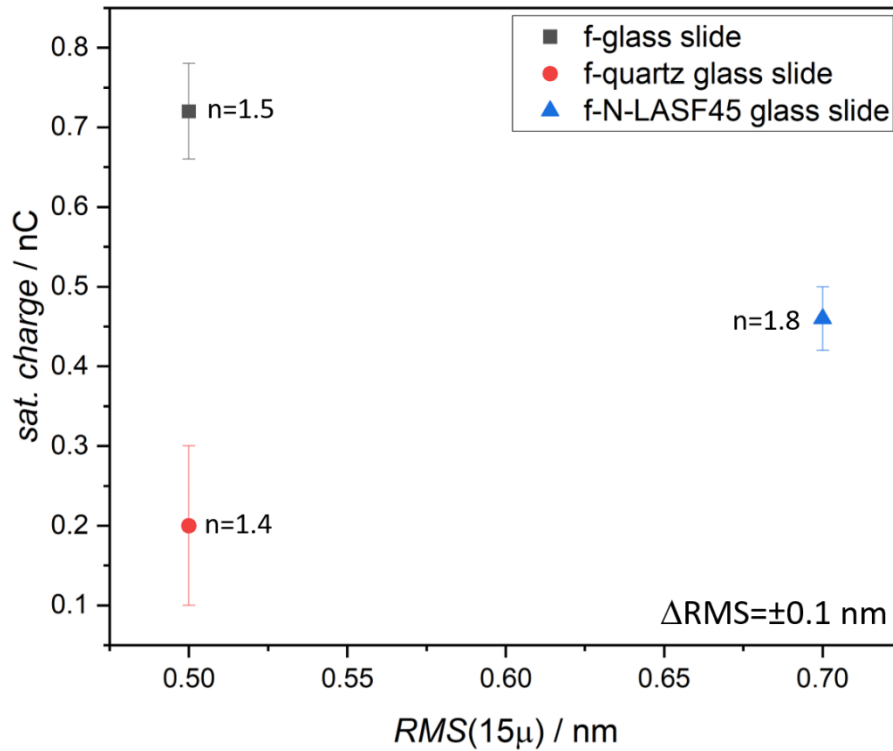


Figure 24: Comparison of different glass substrates to check the influence of the surface chemistry to the drop charge. The saturated drop charge is plotted against the RMS roughness. The RMS roughness was detected at a scan size of  $15\mu$ . The black square show the charge of the f-slide. The red circle shows the drop charge of the fluorinated quartz glass slide and the blue triangle represents the results of the fluorinated N-LASF45 glass substrate. The order of magnitude of the RMS roughness shows that the samples are all in the same range and that an influence of the surface roughness on the drop charge can be neglected. The highest drop charge is shown by the f-slide and the lowest drop charge by the fluorinated quartz glass. It seems that the drop charge is more influenced by the surface chemistry than of the surface roughness. By comparing the refractive index, no correlation between the dielectric constant and the drop charge could be found. The refractive index was taken at a wavelength of 546 nm.

#### 4.3 Influence of roughness on the charge measurement

In the previous section we saw that with increasing surface roughness the drop charge decrease (Figure 23). In this section we will try to answer the question why the drop charge decreases with increasing surface roughness. For this, the wetting properties (chapter 3.9 Contact angle goniometer) and the drop velocity (chapter 3.11 Velocity measurements) were analyzed. The contact area could not be measured in this work.

To compare the wetting properties the ACA and RCA were measured. The three different glass slides with different chemical composition were analyzed. The f-slide with the smoothest and roughest surface were measured and analyzed too. The results are summarized Table 5 and Figure 25.

Table 5: Results of the contact angle measurements. The static contact angle (SCA), advancing contact angle (ACA) and the receding contact angle (RCA) of the different glass substrates and the f-slide with the roughest surface were measured. The contact angle hysteresis was calculated. The error was calculated using standard deviation. The RMS roughness was calculated at a scan size of 500  $\mu$ . The error of the RMS roughness can be found in Table 4.

Sample	RMS / nm	SCA / °	$\Delta$ SCA / °	ACA / °	$\Delta$ ACA / °	RCA / °	$\Delta$ RCA / °	Hysteresis / °	$\Delta$ Hyster. / °
Quartz glass slide	0.8	115	$\pm 4$	116	$\pm 2$	83	$\pm 2$	33	$\pm 3$
N-LASF45 glass slide	0.6	135	$\pm 2$	135	$\pm 3$	88	$\pm 1$	46	$\pm 3$
f-slide	1.1	119	$\pm 1$	119	$\pm 1$	101	$\pm 3$	18	$\pm 3$
f-slide	499	126	$\pm 2$	129	$\pm 1$	98	$\pm 2$	31	$\pm 2$

In Figure 25 the ACA and RCA is plotted against the saturated drop charge. A comparison of the ACA/RCA and the drop charge show us that there is no clear correlation between the drop charge and the contact angle. It can be observed that the sample with the smallest CAH has the largest charge. A clear tendency between CAH and the drop charge is not present here.

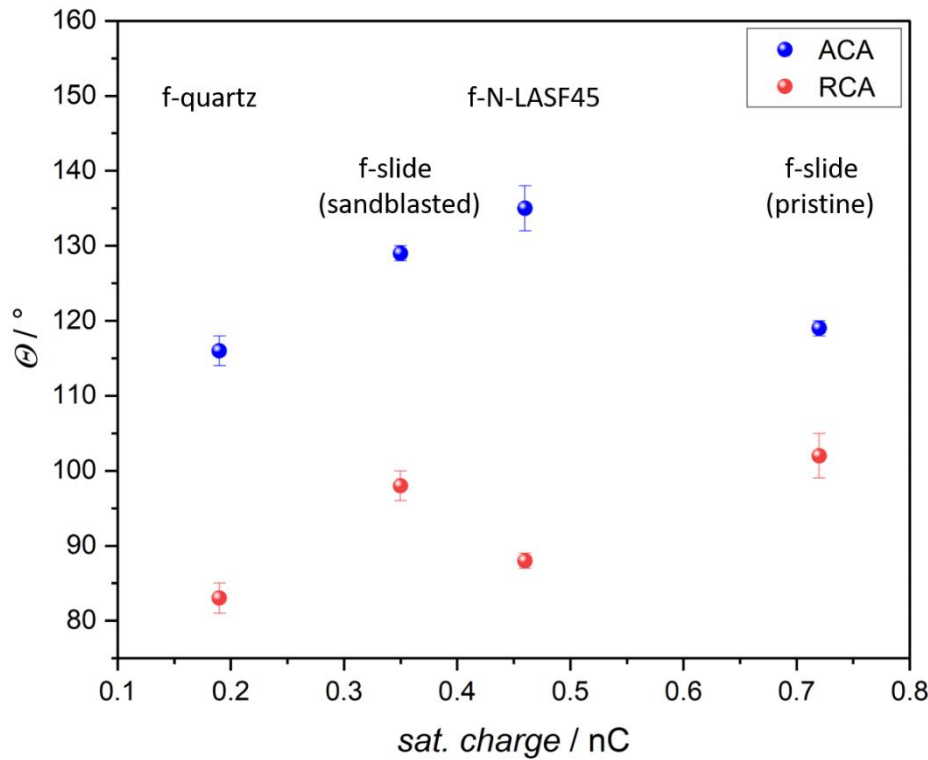


Figure 25: Plot of the advancing contact angle (ACA) and receding contact angle (RCA) against the saturated drop charge of different samples. The blue data marks represent the ACA and the red marks show the RCA. The sample with the smallest contact angle hysteresis (CAH) shows the highest drop charge. A comparison between the different kind of fluorinated glass substrates and the f-slides with different surface roughness show no correlation between the ACA/RCA/CAH and the drop charge.

Results of the velocity measurements are summarized in Figure 26. The *RMS* roughness calculated at a scan size of 500  $\mu$  was used here (chapter 4.1.5 Results and discussion of the calculated *RMS* roughness). The velocity measurement was taken at two different areas on the sample.

A comparison of the plots in Figure 26 shows that the drop velocity decrease with increasing surface roughness. In relation to the drop charge, this means that with decreasing velocity the drop charge decrease. A possible explanation is that the kinetic energy of the drop on the smoother surface is larger and so the drop charge increases. A comparison of the contact time shows that the drop charge decreases with increasing contact time. That could be due to the friction force between drop and surface. With increasing surface roughness the surface area and the friction force increase and the velocity decrease. The longer contact time allows the droplet to interact with the surface longer and the drop charge decrease. A possible effect would be that dissociated charges of water have more time to recombine and thus less charges are deposited. The longer contact time should not be due to the Coulomb force between drop and surface. In this case, a longer contact time would indicate a higher drop charge.

The question remains whether the *RCA* can explain the decreasing drop charge with increasing surface roughness. In the scope of this master thesis this question remains open.

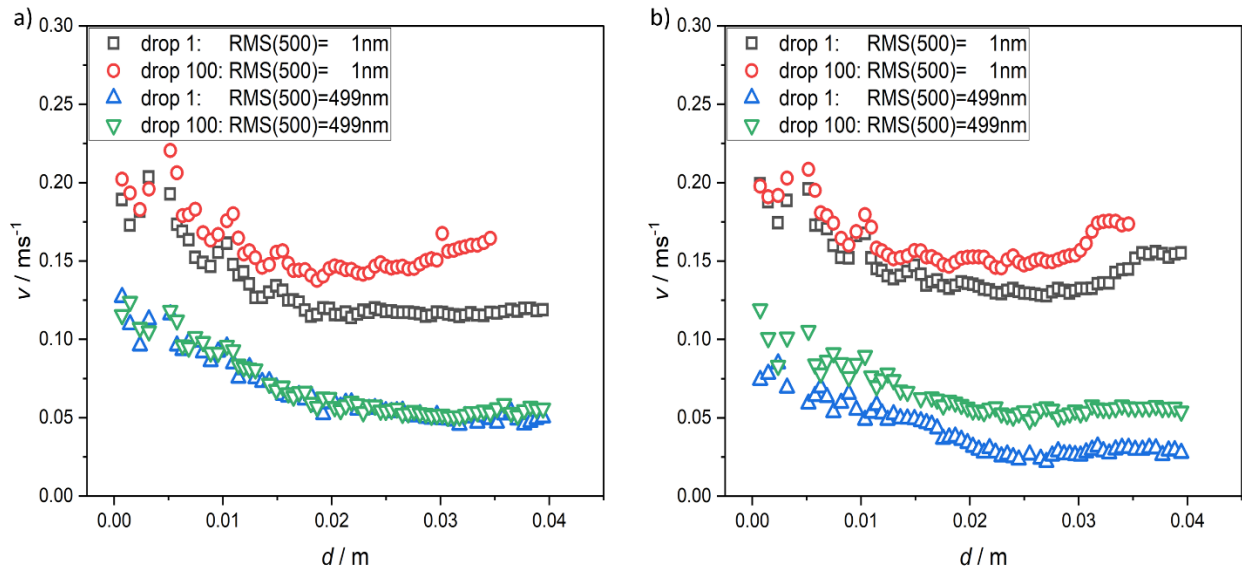


Figure 26: These plots represents the results of the velocity measurement of a water drop at glass surfaces with different surface roughness. The RMS values were calculated at a scan size of  $500 \mu$ . The drop velocity of the first and 100<sup>th</sup> drop is shown. The measurement were done at two different areas of the surfaces. The left panel a) shows the results of the first run. The velocity of two different samples are shown. The surfaces differ in their surface roughness. The right panel b) shows the second run of the experiment. A comparison of the results show that the velocity of the first drop is smaller than the velocity of the 100<sup>th</sup> drop. In relation to the drop charge the results showed that the sample with the higher drop velocity had the higher drop charge. Possible measurement error could be that the base line (manually placed) are not identical in all measurements (inhomogeneous surface) and therefore the polynomial fit used in the evaluation does not fit the same outline of the drops.



## Chapter V: Summary

### 5.1 Conclusion

In my master thesis the influence of the surface roughness on the charging of water drops moving over glass surfaces was investigated. Different kinds of glass slides were used as substrate. The used glass slides were “Menzel” glass slides, quartz glass slides and N-LASF45 glass slides. The glass slides differed in chemical composition.

The first part of the work was to experiment with different methods to change the surface roughness. Changing the surface roughness was done with etching, coating the substrate with silica particles, grinding with SiC-sandpaper and sandblasting the glass slides. Determination of the surface roughness was done with *AFM* and *profilometer*. For evaluation the *RMS* roughness was used to compare the surface roughness of the prepared surfaces. To measure the drop charge of the water drops the glass slides were fluorinated.

It has been shown that both the surface roughness and the surface chemistry of the substrate influence the drop charge. In order to investigate the influence of the surface roughness and surface chemistry separately, the surface roughness was changed while maintaining the surface chemistry. It could be shown that with increasing surface roughness the drop charge decrease. To investigate the question of the influence of the surface roughness in more detail, the drop speed was measured. With decreasing drop velocity the drop charge decrease.

The influence of the surface chemistry could be shown by comparing different glass substrates with different chemical compositions. The surface roughness of the substrates were in the same order of magnitude. As the number of ionic compounds in the glass substrates increased, an increase in the drop charge was observed. In this way, in addition to the surface roughness, the influence of the surface chemistry on the drop charge could be demonstrated.

### 5.2 Outlook

In this work we were able to demonstrate that the influence of surface roughness is small or at least comparable in comparison to the influence of the surface chemistry. The first question that is relevant for further research is whether there is one specific chemical composition in the slides which increase the charge or the sum of the ionic components in the glass slide. The challenge will be find a substrate whose chemical composition can be changed easily. Also it is possible to study the influence of the chemical components by coating the surface with particles. In this case coating with different nanoparticles would be very interesting.

All in all further research in the topic of the surface chemistry and the role of ionic components could contribute a better understanding of charge separation on solid surfaces.

## CHAPTER VI: Chemicals

*Table 6: In this table all used chemicals are summarized.*

Chemical	Company	Purity	CAS-number
Ethanol	Honeywell	absolute	64-17-5
Potassium hydroxide	Carl Roth GmbH + Co. KG	≥85 %	1310-58-3
Tetraethyl orthosilicate	Sigma Aldrich	≥99 %	78-10-4
Ammonia solution	VWR	28%	1336-21-6
Methanol	VWR	absolute	67-56-1
Hydrochloride acid	Sigma Aldrich	≥37 %	7647-01-0
Trichloro(1H,1H,2H,2H-perfluorooctyl)silane	Alfa Aesar	≥97 %	78560-45-9

## Chapter VII: Lists

### [7.1 List of abbreviations](#)

*ACA*: Advancing contact angle

*AFM*: Atomic force microscopy

*CA*: Contact angle

*CAH*: Contact angle hysteresis

*CVD*: Chemical vapor deposition

*EtOH*: Ethanol

*KOH*: Potassium hydroxide

*MeOH*: Methanol

*PFTE*: Polytetrafluoroethylene

*PFOTS*: 1H, 1H, 2H, 2H-Perfluorooctyltrichlorosilane

*RCA*: receding contact angle

*RMS*: root mean square

*TENG*: triboelectric nanogenerator

## 7.2 List of figures

**Figure 1:** Illustration of the surface roughness. a) The surface was measured with the AFM at a scan size of 15  $\mu$ . Along two lines in the image (red and white line) a height profile was recorded as shown in b). The red plot corresponds to the red line in a) (RMS roughness=31.2 nm). The black plot in b) corresponds to the white line in a) (RMS roughness=4.7 nm). A comparison of these two profiles in b) shows that the surface roughness is dependent both on the point of the measurement and the scan size. The scan size has always be cited to make the results comparable. A number for the surface roughness can be calculated from the high profile. Here are different methods of the calculation of the surface roughness possible. .... 3

**Figure 2:** Schematic illustration of the definitions of the contact angle, the advancing and receding contact angle and the wetting state in dependence on the surface roughness. a) Represents the Young model, which is used to describe the wetting properties with the contact angle ( $\theta_{CA}$ ) and the surface tension  $\gamma$ . The contact angle is the angle between the surface and the front of the water drop, when the drop is in a thermodynamic equilibrium. The thermodynamic equilibrium means that the surface tension between the three media solid, air (vapor) and liquid ( $\gamma_{SV}$ - surface tension solid-vapor;  $\gamma_{LV}$ - surface tension liquid-vapor and  $\gamma_{SL}$ -surface tension solid-liquid) are in an energetic equilibrium state. The Young model describes ideal surfaces. b) Advancing (ACA) and the receding contact angle (RCA) of a moving drop. The right drop front represents the front in which the drop moves. The maximum contact angle is called ACA ( $\theta_{ACA}$ ). On the left side, we see the angle form the front which is receding. The angle at which the droplet starts to move is the RCA ( $\theta_{ACA}$ ). Under consideration of the surface roughness, there are two different states of wetting possible. c) Shows the Wenzel state. In this state no air is between drop and surface. d) Shows the Cassie-Baxter state. In this case air is between the surface and the drop.<sup>[27]</sup> ..... 5

**Figure 3:** Schematic illustration of the electrical double layer (Gouy-Chapman-Stern model). The green bar on the left side represents the solid. Blue background represents the liquid medium (e.g. water). The yellow, green and purple spheres represent the neutral species, the anions and the cations. The ions are solvated by water molecules (red: oxygen, white: hydrogen). The inner Helmholtz plane (IHP) describes the interaction between the surface of the solid and the liquid medium. In fact, of the surface charge counter ions and counter charge bind to the surface to neutralize the charge. Also, solvent molecules like the water molecules can adhere to the surface to neutralize the surface charge. The outer Helmholtz plane (OHP) describes the interaction of solvated molecules with the IHP. Together, these both layers form the so called Stern layer. The Stern layer is bordered by the diffuse layer. Since the ions or solvated molecules diffuse from the Stern layer to the diffuse layer and vice versa a

potential  $\phi$  can be described as a function of the thickness of the Stern layer ( $d$ ) and the distance from the surface. The diffuse layer is also called Debye length ( $\kappa^{-1}$ ).<sup>[35]</sup> ..... 8

**Figure 4:** Calculation of the drop charge. The results of the drop charge measurement of 500 water drops sliding over a fluorinated glass slide surface should serve as an example. During the measuring the current of each drop is measured with an electrode. a) Detected current signal for drop number: 1, 50, 100, 200, 400, 500. With an increasing drop number the current of the drop first decrease till the current takes on a constant value around drop number 200. Furthermore follows from the plot the discharging time of the drop at the electrode. The whole discharging time of the drop is around 20 ms. For the calculation of the drop charge, the current signal is integrated over the time ( $Q = \int I(t) dt$ ). The time interval for the integration is given by the discharging time of the current peak (around 0.2 ms). b) The calculated drop charge is plotted against the drop number. With an increasing drop number the drop charge decrease till the drop charge reach a constant value. The drop charge at this point is called saturation charge (saturated charge) (blue circle). ..... 9

**Figure 5:** Schematic model for the description of the slide electrification. The model is divided into three steps to explain the whole charging process of a water drop sliding down a hydrophobic surface. (1) The interaction between the droplet and the solid surface leads to the formation of an electric double layer. (2) Charges are transferred to the surface. When the drop continues to slide the charges remain on the surfaces. (3) The surface charge can be neutralized through various possibilities. The neutralization of the charge can be done by e.g. by ions from the air, interaction with the next drop or by flow of electrons through the grounded substrate.<sup>[15]</sup> ..... 10

**Figure 6:** Schematic diagram of the fluorination of quartz glass. The fluorination reagent is 1H,1H,2H,2H-perfluorooctyltrichlorosilane (**PFOTS**). First, hydrolysis of the PFOTS lead to the elimination of hydrogen chloride (HCl). The hydroxide group of the PFOTS can now interact with hydroxide groups of the quartz-glass. Water (H<sub>2</sub>O) is released as bye-product in this process (condensation). Also condensation is then used to bond the silane chains between each other to the glass surface. .... 11

**Figure 7:** AFM images of a) pristine and b) fluorinated slide. The pattern (e.g. red and blue circle) on these images were observed on all measured slides. A comparison of the pattern in a) and b) shows that the surface structures from slide to slide are different. Furthermore the comparison between a) and b) shows that the fluorination has no visible influence to the surface structure and such an influence to the surface roughness can be neglected (RMS roughness from a) and b) are in the same order of magnitude ((0.5±0.1) nm)). The images were recorded at a scan size of 15  $\mu$ ..... 13

<b>Figure 8:</b> AFM images of a) quartz glass slide and b) N-LASF45 glass slide. The images were recorded at a scan size of 15 $\mu$ . In contrast to the “Menzel” glass slides no different patterns are visible (see Figure 7). The calculated RMS roughness is for a) (0.5 $\pm$ 0.1) nm) and b) (0.7 $\pm$ 0.1) nm).....	14
<b>Figure 9:</b> The fluorination was analyzed by AFM. The surface of the slide was detected after slide pre-preparation and before fluorination (a)). After one hour fluorination the slide was taken out of the desiccator and measured again (b)). Here an influence of fluorination to the surface is visible, some particle-like structures are visible. These structures could be by-products or non-reacted components of the reaction. After rinsing the surface with ethanol and DI water no by-products are observed at the fluorinated surface and further analysis showed a probably monomolecular layer of PFOTS on the slide (c)).....	15
<b>Figure 10:</b> Experimental setup of the experiment “grinding with sandpaper”. During the first experiments it was observed that the edges of the slides were stronger grinded than the rest of the surface or the slide was even broken. To protect the edges four slides were added around the sample (a)). Than the surface was grinding by pulling the grinding block with the cord (b)). .....	17
<b>Figure 11:</b> Experimental setup of charge measurement. (1) Faraday cage. (2) Aluminum plate. (3) Rotatable holder. (4) Needle. (5) Laser pointer. (6) Photodiode. (7) Sample and sample holder. (8) Current amplifier. (9) Vessel. (10) Ionic air blower. ....	19
<b>Figure 12:</b> Schematic drawing of the charge measurement setup. For a better overview the scheme is given from a top view. All metal parts are grounded and connect to the Faraday cage (1). The sample is fixed on the sample holder (2). The sample holder can be rotated to adjust the tilt angle (3, not shown here). The needle (4) is connected to a peristaltic pump. The drop height as well the speed of the pump can varied. With the laser (5) a voltage can be measured by the photodiode (6) by reflection of the laser beam at the surface of the sample. The electrode (7) is connected to a current amplifier to detect the charge of the sliding drop. ....	20
<b>Figure 13:</b> Advancing (ACA) and receding (RCA) contact angle of a water drop on a fluorinated N-LASF45 glass slide. Plot of the contact angle against the frame number. After the drop is placed on the surface, the drop volume is increased from 6 to 50 $\mu$ L. Then the drop volume is reduced again to 6 $\mu$ L and the process is repeated again. The contact angle of the drop is recorded by a circle fit during the measurement. During increase of the drop volume, the contact angle reaches a maximum (blue circles). This angle is the ACA. The ACA was calculated by averaging the two plateaus (blue plateaus). In contrast to the ACA, the RCA cannot be determined using a plateau in the plot. The minimum of the plot does not correspond to the definition of the RCA (red circle). The RCA is determined as the point when the drop moves visually. <sup>[24]</sup> .....	22

**Figure 14:** Goniometer DataPhysics OCA35. (1) 100  $\mu$ L Hamilton syringe with needle. (2) Sample and sample holder. The sample holder can be moved with a motor in x,y,z. (3) A Lamp as light source to record and calculated the contact angle with the camera (4). The whole goniometer can be tilted to record roll off angles. .... 23

**Figure 15:** Schematically illustration of the applied polynomial fit during the velocity measurement. After recording the sliding drop by the high speed camera the drop is evaluated with the polynomial fit of fourth degree. A fit is placed over both the drop front (red line) and the drop back side (orange line) of each recording. The contact angle (CA) of the drop front ( $CA_f$ ) and the drop back side ( $CA_b$ ) is calculated. The  $CA_f$  is the advancing contact angle during movement. The  $CA_b$  is the receding contact angle during movement. The velocity from the drop front and drop back side is also calculated by the polynomial fit. .... 24

**Figure 16:** Experimental setup of the velocity measurement of the water drops. (1) Experimental setup is fixed at a plate that can be rotated to change the tilt angle. (2) Sample holder. (3) Syringe. (4) High speed camera. .... 24

**Figure 17:** Influence of etching with KOH on the surface roughness of the slide under different conditions. Images were recorded with the AFM. The RMS roughness were calculated at a scan size of 15  $\mu$  (AFM) and 500  $\mu$  (profilometer). a) Pristine fluorinated slide, b) etched slide at pH 12 and 2 days etching time, c) etched slide at pH 12 and 7 days etching time, d) etched slide at pH 14 and 2 days etching time, e) etched slide at pH 14 and 7 days etching time. All images show the surface structures of a pristine slide (blue circles). That means the influence of etching with KOH is small. This is also evident from the calculated RMS values..... 26

**Figure 18:** AFM images and calculated RMS roughness of the sandblasted slides at different pressure. a) Sandblasted at 1.5 bar,  $RMS(500\mu)=(104\pm71)$  nm,  $RMS(15\mu)=(9\pm6)$  nm. b) Sandblasted at 2.0 bar,  $RMS(500\mu)=(498\pm315)$  nm,  $RMS(15\mu)=(105\pm39)$  nm. In both experiments the surface changed visibly. The surface roughness increased with the pressure of the sandblasting. The errors show that by sandblasting the surface roughness is changed inhomogeneous..... 27

**Figure 19:** AFM images and calculated RMS values of the slides after grinding with different SiC sandpaper: a) Label P80, grit size 221  $\mu$ m b) P280, grit size 52  $\mu$ m c) P800, grit size 22  $\mu$ m d) P1500, grit size 13  $\mu$ m. In all AFM images grooves are visible. The distance between the grooves is dependent on the used size auf SiC particle at the sandpaper (red circles). There are areas of the surface where the influence of the grinding is small. In this areas the typical surface structures of a pristine slide are visible (blue circle)..... 28

**Figure 20:** a) AFM image and calculated RMS values of the slide coated with silica particle (particle size: 108 nm). Between the silica particles vacancies are visible b) AFM image and calculated RMS values of

the slide coated with silica particle (particle size: 399 nm). There are almost no vacancies and the particles are piling up. c) AFM image and calculated RMS values of the slide coated with silica particle (mixed particle size). Multiple layers of particles are visible. d) Camera picture of a sample coated with silica particle. The picture was taken with the camera of the profilometer. With the crosshair the measuring point can be chosen. The black arrow illustrates the scan size of 500  $\mu$ . It is obvious that the surface roughness depends on the measurement point. .... 29

**Figure 21:** Results of the drop charge measurement in consideration of the surface roughness. The RMS roughness was calculated at a scan size of 15  $\mu$ . a) Plot of the measured drop charge against the drop number. The dashed line represent the drop charge which was used for the saturated drop charge. b) Saturated drop charge against the RMS roughness. With increasing surface roughness the drop charge decreases. a) We see two different surfaces with a RMS roughness of 9 nm. The surface roughness of these both samples were changed by different methods (sandblasting and grinding with sandpaper). A comparison of the two surfaces with the naked eye showed that the surface roughness are different. It can be concluded that the scan size of 15  $\mu$  used is too small and therefore the calculated RMS values do not reflect the actual surface roughness. The error bars correspond to the standard deviation. .... 32

**Figure 22:** Results of the drop charge measurement in consideration of the surface roughness. The RMS roughness was calculated at a scan size of 500  $\mu$ . a) Plot of the measured drop charge against the drop number. The dashed line represents the drop charge which was used for the saturated drop charge. b) Plot of the saturated drop charge against the RMS roughness. On the one hand we see that the drop charge decrease with increasing surface roughness. On the other hand we find in the range from 0 to 100 nm the minimum and maximum of drop charge. To understand this, the method with which the surface roughness was changed were compared (orange circles in b)). It turned out that in the samples where the surface roughness was changed mechanically (non-coated with silica particle) the drop charge decrease with increasing RMS roughness. It is different with the samples that have been coated with silica particle. Both the surface roughness and surface chemistry was changed here. It seems that apart from the surface roughness the surface chemistry or the chemical composition of the substrate influences the drop charge. The error bars correspond to the standard deviation. .... 33

**Figure 23:** The saturated drop charge is plotted against the RMS roughness. The calculation of the RMS roughness was done at a scan size of 500  $\mu$ . To compare the influence of the surface roughness and the surface chemistry of the substrate on the drop charge, two different types of sample were used. The black data marks represent the f-slides as substrate with different surface roughness. The surface roughness was changed mechanically and so the surface chemistry of these samples should be similar. The red marks show the results of the f-slides which were coated with silica particle. Next to the surface



roughness the surface chemistry of the substrate was changed here. If we compare the results separately we see the following: For the non-coated (silica particle) f-slides the drop charge decrease with increasing surface roughness (black marks). The red marks show no relationship between drop charge and surface roughness. Reason could be that the RMS roughness for inhomogeneous surfaces are not so clear. If we compare two samples with similar surface roughness but different surface chemistry we see the (orange circle) that the drop charge of these two samples is different. It can be assumed that next to the surface roughness the surface chemistry influence the drop charge. .... 34

**Figure 24:** Comparison of different glass substrates to check the influence of the surface chemistry to the drop charge. The saturated drop charge is plotted against the RMS roughness. The RMS roughness was detected at a scan size of  $15\mu$ . The black square show the charge of the f-slide. The red circle shows the drop charge of the fluorinated quartz glass slide and the blue triangle represents the results of the fluorinated N-LASF45 glass substrate. The order of magnitude of the RMS roughness shows that the samples are all in the same range and that an influence of the surface roughness on the drop charge can be neglected. The highest drop charge is shown by the f-slide and the lowest drop charge by the fluorinated quartz glass. It seems that the drop charge is more influenced by the surface chemistry than of the surface roughness. By comparing the refractive index, no correlation between the dielectric constant and the drop charge could be found. The refractive index was taken at a wavelength of 546 nm..... 36

**Figure 25:** Plot of the advancing contact angle (ACA) and receding contact angle (RCA) against the saturated drop charge of different samples. The blue data marks represent the ACA and the red marks show the RCA. The sample with the smallest contact angle hysteresis (CAH) shows the highest drop charge. A comparison between the different kind of fluorinated glass substrates and the f-slides with different surface roughness show no correlation between the ACA/RCA/CAH and the drop charge. 38

**Figure 26:** These plots represents the results of the velocity measurement of a water drop at glass surfaces with different surface roughness. The RMS values were calculated at a scan size of  $500\mu$ . The drop velocity of the first and 100<sup>th</sup> drop is shown. The measurement were done at two different areas of the surfaces. The left panel a) shows the results of the first run. The velocity of two different samples are shown. The surfaces differ in their surface roughness. The right panel b) shows the second run of the experiment. A comparison of the results show that the velocity of the first drop is smaller than the velocity of the 100<sup>th</sup> drop. In relation to the drop charge the results showed that the sample with the higher drop velocity had the higher drop charge. Possible measurement error could be that the base line (manually placed) are not identical in all measurements (inhomogeneous surface) and therefore the polynomial fit used in the evaluation does not fit the same outline of the drops. .... 39

<b>Figure 27:</b> Recorded SEM images of the surface of the slides coated with silica particle. With the help of the SEM images and the software ImageJ the particle size was calculated (yellow slines). a) Silica particle A with a size of $108\pm19$ nm. b) Silica particle with a size of $399\pm28$ nm.....	53
<b>Figure 28:</b> Results of the charge measurements for the etching experiments in depends of the calculated surface roughness. As reference serve the result of the fluorinated slide (purple plot). Under consideration of the error bars (standard deviation) no influence of etching to the charge measurement can be observed. Resulting plots with a calculated roughness at a scan size of a) $15\times15\text{ }\mu\text{m}$ b) $500\text{ }\mu\text{m}$ . ....	53
<b>Figure 29:</b> Results of the charge measurements for the sandblasted samples and fluorinated slide. a) Results at a scan size of $15\times15\text{ }\mu\text{m}$ . b) Results at a scan size of $500\text{ }\mu\text{m}$ .....	54
<b>Figure 30:</b> Results of the charge measurements for the SiC-sandpaper gridnded samples and fluorinated slide. a) Results at a scan size of $15\times15\text{ }\mu\text{m}$ . b) Results at a scan size of $500\text{ }\mu\text{m}$ . ....	54
<b>Figure 31:</b> Camera picture of different surfaces. The picture was taken with the camera of the profilometer. a) Shows the surface of a sandblasted slide with a pressure of 2.0 bar. b) Shows the surface of a slide which was grinded with SiC sandpaper (P800). With the crosshairs and the blue arrow the measuring point can be chosen. The black arrow illustrates the scan size of $500\text{ }\mu\text{m}$ . It is obvious that the surface roughness depends the measuring point. ....	55
<b>Figure 32:</b> These plots show the results of the experiments of the velocity of a water drop on glass surfaces with different surface roughness. The RMS values were calculated with the AFM at a scan size of $15\times15\text{ }\mu\text{m}$ . The experiment was done two times at two different surface areas. a) Show the results of the first run and b) show the results of the second run. In both experiments we can see that the drop velocity decrease with increasing surface roughness. ....	55

### 7.3 List of tables

<b>Table 1:</b> The chemical components of the microscopic slides (Thermo Fisher scientific Gerhard Menzel B.V. & Co. KG). .....	12
<b>Table 2:</b> Approach of the synthesis of silica particle. Also listed are the determined particle sizes and the concentration of the solution. The error $\Delta d$ is the standard deviation. The error of the concentration represents the error of the scale .....	16
<b>Table 3:</b> Approach of the etching series. The slides were etched in KOH solutions. The error of the weighted-in quantity corresponds to the error of the scale and the error of the volume corresponds to the error of the glass device.....	16
<b>Table 4:</b> Calculated surface roughness (RMS) of all samples. The RMS roughness was calculated at a scan size of 15 x 15 $\mu\text{m}$ with the AFM and 500 $\mu\text{m}$ with the profilometer. The error was calculated by standard division. ....	30
<b>Table 5:</b> Results of the contact angle measurements. The static contact angle (SCA), advancing contact angle (ACA) and the receding contact angle (RCA) of the different glass substrates and the f-slide with the roughest surface were measured. The contact angle hysteresis was calculated. The error was calculated using standard deviation. The RMS roughness was calculated at a scan size of 500 $\mu\text{m}$ . The error of the RMS roughness can be found in Table 4. ....	37
<b>Table 6:</b> In this table all used chemicals are summarized. ....	41

## Chapter VIII: Literature

### 8.1 References

- [1] L. E. Helseth, *Applied Energy* **2021**, 300, 117394.
- [2] W. Xu, H. Zheng, Y. Liu, X. Zhou, C. Zhang, Y. Song, X. Deng, M. Leung, Z. Yang, R. X. Xu, *Nature* **2020**, 578, 392-396.
- [3] G. Zhu, Z.-H. Lin, Q. Jing, P. Bai, C. Pan, Y. Yang, Y. Zhou, Z. L. Wang, *Nano letters* **2013**, 13, 847-853.
- [4] J. K. Moon, J. Jeong, D. Lee, H. K. Pak, *Nature communications* **2013**, 4, 1-6.
- [5] X.-S. Zhang, M.-D. Han, R.-X. Wang, F.-Y. Zhu, Z.-H. Li, W. Wang, H.-X. Zhang, *Nano letters* **2013**, 13, 1168-1172.
- [6] C. Wu, A. C. Wang, W. Ding, H. Guo, Z. L. Wang, *Advanced Energy Materials* **2019**, 9, 1802906.
- [7] Z.-H. Lin, G. Cheng, W. Wu, K. C. Pradel, Z. L. Wang, *ACS nano* **2014**, 8, 6440-6448.
- [8] Z. H. Lin, G. Cheng, L. Lin, S. Lee, Z. L. Wang, *Angewandte Chemie International Edition* **2013**, 52, 12545-12549.
- [9] S. Pan, Z. Zhang, *Friction* **2019**, 7, 2-17.
- [10] J. E. Lawver, *Journal of the Electrochemical Society* **1969**, 116, 57C.
- [11] D. J. Lacks, R. M. Sankaran, *Journal of Physics D: Applied Physics* **2011**, 44, 453001.
- [12] F. Di Giacomo, *Introduction to Marcus Theory of Electron Transfer Reactions*, World Scientific, **2020**.
- [13] B. Persson, M. Scaraggi, A. Volokitin, M. Chaudhury, *EPL (Europhysics Letters)* **2013**, 103, 36003.
- [14] H. Baytekin, A. Patashinski, M. Branicki, B. Baytekin, S. Soh, B. A. Grzybowski, *Science* **2011**, 333, 308-312.
- [15] A. Z. Stetten, D. S. Golovko, S. A. Weber, H.-J. Butt, *Soft Matter* **2019**, 15, 8667-8679.
- [16] W. S. Wong, P. Bista, X. Li, L. Veith, A. Sharifi-Aghili, S. A. Weber, H.-J. r. Butt, *Langmuir* **2022**.
- [17] H. Y. Erbil, *Surface chemistry of solid and liquid interfaces*, Wiley-Blackwell, **2006**.
- [18] T. Thomas, *Precision Engineering* **1981**, 3, 97-104.
- [19] N. Myers, *Wear* **1962**, 5, 182-189.
- [20] B. Voigtländer, *Scanning probe microscopy: Atomic force microscopy and scanning tunneling microscopy*, Springer, **2015**.
- [21] L. E. Helseth, *Langmuir* **2019**, 35, 8268-8275.
- [22] H. J. Butt, K. Graf, M. Kappl, *Physics and Chemistry of Interfaces*, Wiley, **2006**.
- [23] M. Rankl, S. Laib, S. Seeger, *Colloids and surfaces B: Biointerfaces* **2003**, 30, 177-186.
- [24] T. Huhtamäki, X. Tian, J. T. Korhonen, R. H. Ras, *Nature protocols* **2018**, 13, 1521-1538.
- [25] C. Neinhuis, F. Groß, L. Elfenthal, S. Blöß, R. Grau, M. Fleisch, D. Bahnemann, *Chemie in unserer Zeit* **2014**, 48, 92-100.
- [26] W. A. Zisman, ACS Publications, **1964**.
- [27] Z. Chu, S. Seeger, *Chemical Society Reviews* **2014**, 43, 2784-2798.
- [28] C. Dorrer, J. Rühle, *Langmuir* **2006**, 22, 7652-7657.
- [29] H.-J. r. Butt, R. d. Berger, W. Steffen, D. Vollmer, S. A. Weber, *Langmuir* **2018**, 34, 11292-11304.
- [30] K. Liu, L. Jiang, *Annual Review of Materials Research* **2012**, 42, 231-263.
- [31] R. N. Wenzel, *Industrial & Engineering Chemistry* **1936**, 28, 988-994.
- [32] A. B. D. Cassie, S. Baxter, *Transactions of the Faraday Society* **1944**, 40, 546-551.
- [33] G. Wedler, *Lehrbuch der Physikalischen Chemie*, Wiley, **2005**.
- [34] H. v. Helmholtz, *Annalen der Physik* **1879**, 243, 337-382.
- [35] G. Gonella, E. H. Backus, Y. Nagata, D. J. Bonthuis, P. Loche, A. Schlaich, R. R. Netz, A. Kühnle, I. T. McCrum, M. Koper, *Nature Reviews Chemistry* **2021**, 5, 466-485.
- [36] P. Atkins, J. De Paula, *Atkins' Physical Chemistry*, Macmillan Higher Education, **2006**.

- [37] E. Riedel, C. Janiak, *Anorganische chemie*, de Gruyter, **2022**.
- [38] Satorius.
- [39] P. Vogel, N. Möller, P. Bista, H.-J. Butt, B. Liebchen, T. Palberg, *arXiv preprint arXiv:2201.11029* **2022**.
- [40] A. F. Holleman, N. Wiberg, *Grundlagen und Hauptgruppenelemente*, Walter de Gruyter GmbH & Co KG, **2016**.
- [41] U. Riebesell, *Journal of Oceanography* **2004**, *60*, 719-729.
- [42] F. Darvish, *private communication*.
- [43] Z. H. Lin, G. Cheng, S. Lee, K. C. Pradel, Z. L. Wang, *Advanced Materials* **2014**, *26*, 4690-4696.
- [44] J. Brzoska, I. B. Azouz, F. Rondelez, *Langmuir* **1994**, *10*, 4367-4373.
- [45] J. Cras, C. Rowe-Taitt, D. Nivens, F. Ligler, *Biosensors and bioelectronics* **1999**, *14*, 683-688.
- [46] W.-M. Munief, F. Heib, F. Hempel, X. Lu, M. Schwartz, V. Pachauri, R. Hempelmann, M. Schmitt, S. Ingebrandt, *Langmuir* **2018**, *34*, 10217-10229.
- [47] C. F. Z. G.H Bogush, *Journal of Colloid and Interface Science* **1991**, *142*, 1-18.
- [48] W. Vogel, *G. Chemie*, Springer Verlag, **1992**.
- [49] F. Darvish, N. M. Sarkari, M. Khani, E. Eslami, B. Shokri, M. Mohseni, M. Ebrahimi, M. Alizadeh, C. F. Dee, *Applied Surface Science* **2020**, *509*, 144815.
- [50] A. F. Werner Stöber, Ernst Bohn, *Journal of Colloid and Interface Science* **1968**, *26*, 62-69.
- [51] X. Li, S. Silge, A. Saal, G. Kircher, K. Koynov, R. d. Berger, H.-J. r. Butt, *Langmuir* **2021**, *37*, 1571-1577.
- [52] S. Silge, Technische Universität Darmstadt **2019**.
- [53] N. K. Andersen, R. Taboryski, *Measurement Science and Technology* **2017**, *28*, 047003.
- [54] S. Matsuo, H. Sumi, S. Kiyama, T. Tomita, S. Hashimoto, *Applied surface science* **2009**, *255*, 9758-9760.
- [55] C. Iliescu, J. Jing, F. E. Tay, J. Miao, T. Sun, *Surface and Coatings Technology* **2005**, *198*, 314-318.
- [56] M. J. Kreder, J. Alvarenga, P. Kim, J. Aizenberg, *Nature Reviews Materials* **2016**, *1*, 1-15.

## Chapter IX: Appendix

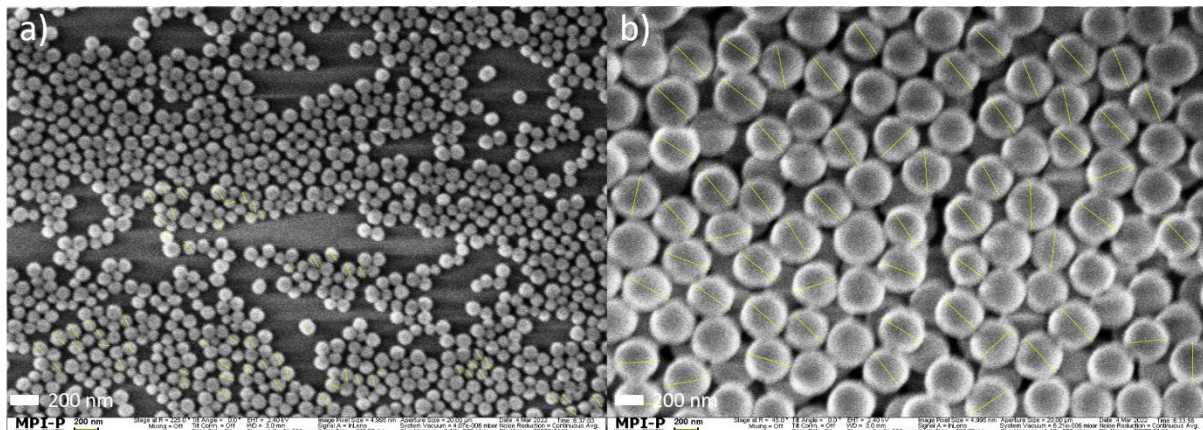


Figure 27: Recorded SEM images of the surface of the slides coated with silica particle. With the help of the SEM images and the software ImageJ the particle size was calculated (yellow slines). a) Silica particle A with a size of  $108 \pm 19$  nm. b) Silica particle with a size of  $399 \pm 28$  nm.

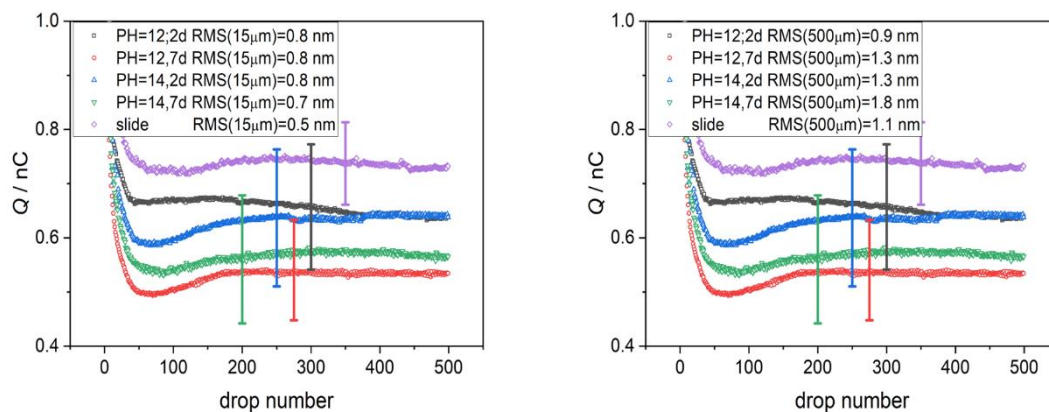


Figure 28: Results of the charge measurements for the etching experiments in depends of the calculated surface roughness. As reference serve the result of the fluorinated slide (purple plot). Under consideration of the error bars (standard deviation) no influence of etching to the charge measurement can be observed. Resulting plots with a calculated roughness at a scan size of a)  $15 \times 15 \mu\text{m}$  b)  $500 \mu\text{m}$ .

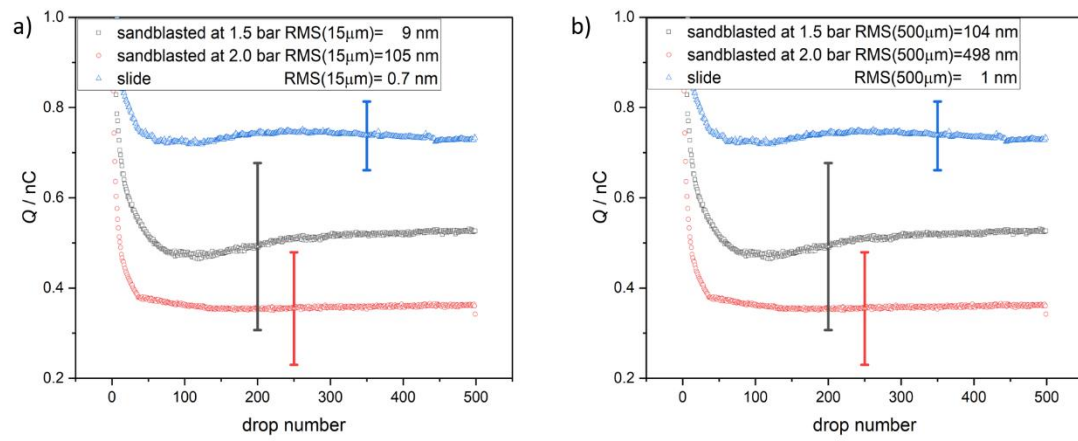


Figure 29: Results of the charge measurements for the sandblasted samples and fluorinated slide. a) Results at a scan size of 15x15  $\mu m$ . b) Results at a scan size of 500  $\mu m$ .

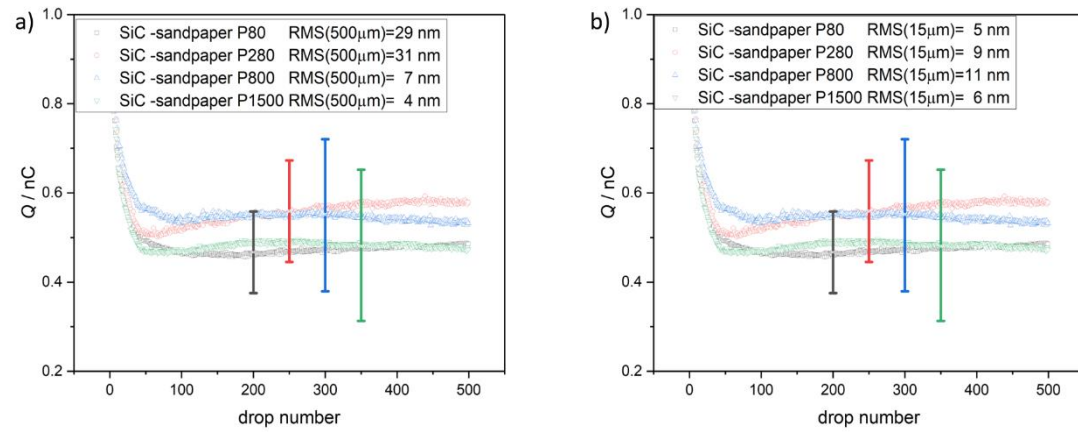


Figure 30: Results of the charge measurements for the SiC-sandpaper gridnded samples and fluorinated slide. a) Results at a scan size of 15x15  $\mu m$ . b) Results at a scan size of 500  $\mu m$ .



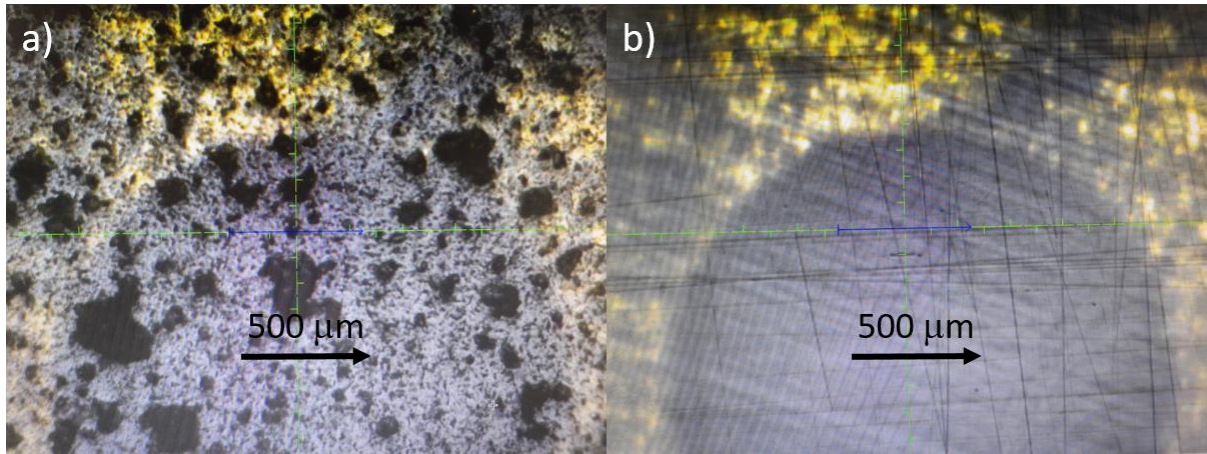


Figure 31: Camera picture of different surfaces. The picture was taken with the camera of the profilometer. a) Shows the surface of a sandblasted slide with a pressure of 2.0 bar. b) Shows the surface of a slide which was grinded with SiC sandpaper (P800). With the crosshairs and the blue arrow the measuring point can be chosen. The black arrow illustrates the scan size of 500  $\mu\text{m}$ . It is obvious that the surface roughness depends the measuring point.

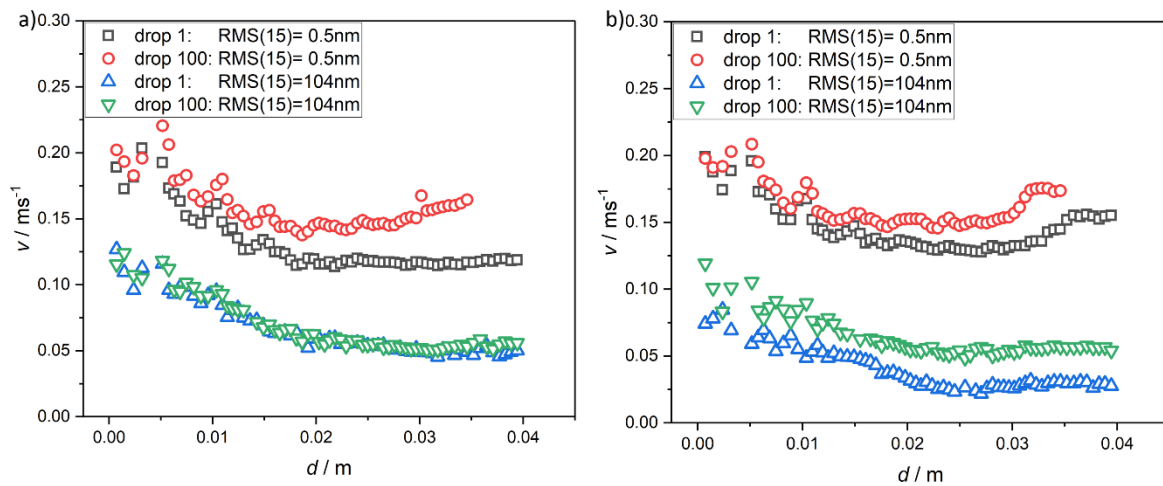


Figure 32: These plots show the results of the experiments of the velocity of a water drop on glass surfaces with different surface roughness. The RMS values were calculated with the AFM at a scan size of 15x15  $\mu\text{m}$ . The experiment was done two times at two different surface areas. a) Show the results of the first run and b) show the results of the second run. In both experiments we can see that the drop velocity decrease with increasing surface roughness.